Speed of sound in humid air: Accurate thermodynamic model and experimental validation

Original
Speed of sound in humid air: Accurate thermodynamic model and experimental validation / Gavioso, R. M.; Astrua, M.; Zucco, M.; Pisani, M.. - In: JOURNAL OF PHYSICAL AND CHEMICAL REFERENCE DATA. - ISSN 0047-2689. - 54:4(2025). [10.1063/5.0294663]

Publisher:
American Institute of Physics

Published
DOI:10.1063/5.0294663

Journal of Physical and Chemical Reference Data

AIP Publishing

RESEARCH ARTICLE | DECEMBER 02 2025

Speed of sound in humid air: Accurate thermodynamic model and experimental validation

R. M. Gavioso ; M. Astrua ; M. Zucco ; M. Pisani

J. Phys. Chem. Ref. Data 54, 043101 (2025)
https://doi.org/10.1063/5.0294663

Journal of Physical and Chemical Reference Data
ARTICLE
pubs.aip.org/aip/jpr

Speed of sound in humid air: Accurate thermodynamic model and experimental validation

Cite as: J. Phys. Chem. Ref. Data **54**, 043101 (2025); doi: 10.1063/5.0294663
Submitted: 5 August 2025 • Accepted: 13 October 2025 •
Published Online: 2 December 2025

R. M. Gavioso,[a] **M. Astrua, M. Zucco, and M. Pisani**

AFFILIATIONS

Istituto Nazionale di Ricerca Metrologica, Strada delle Cacce 91, 10135 Torino, Italy

[a] **Author to whom correspondence should be addressed:** r.gavioso@inrim.it

ABSTRACT

We present a thermodynamic model of speed of sound w in humid air as a function of the parameters of influence namely temperature T, pressure p, relative humidity h_r, carbon dioxide concentration x_{CO2}, and acoustic frequency f. The validity of the model extends between 200 K and 647 K, for pressures up to 10 MPa. By implementing the most accurate thermodynamic information currently available for dry air, water vapor, and their interaction, including heat capacities, virial coefficients and relaxation parameters, the model revises and updates the most complete previous correlation [A. J. Zuckerwar, *Handbook of the Speed of Sound in Real Gases – Volume III Speed of Sound in Air* (Academic Press, London, 2002)], reducing its relative standard uncertainty by more than one order of magnitude, down to 25 ppm at ordinary, near-ambient conditions. The software implementation of the model is made available by publication of source and executable files To test the validity of the model and its practical application, we have measured the speed of sound in humid air near ambient pressure using an acoustic wavelength meter set up in a hemi-anechoic chamber and compared a subset of these experimental determinations with those obtained by flowing air, sampled from the same environment, through a spherical resonator. The results from both experiments were found consistent with the model within their combined uncertainties. The positive outcome of the comparison suggests that acoustic thermometry in humid air may be realized at the level of 0.015 K with perspectives for application to dimensional measurements, temperature and acoustic metrology, and atmospheric physics.

CONTENTS

List of Tables

List of Figures

1. Introduction

Besides the importance of speed of sound in air as a fundamental thermodynamic property of a fluid of utmost scientific and technological interest, the achievement of accurate theoretical predictions and measurements of speed of sound in air are essential for the development of several metrological applications. For instance, the acoustic determination of air temperature along the optical path of an interferometer has been previously demonstrated to be an effective method to estimate the corrections required to account for the temperature dependence of the optically measured refractive index.[1] Also, sonic anemometers, which are instruments widely used in meteorology, are designed to measure the temperature of air, in addition to wind velocity, to investigate turbulent heat flow in the atmospheric boundary layer.[2]

In these applications of acoustic thermometry, the ultimate achievable accuracy is limited by the uncertainty of the model used to calculate the dependence of the speed of sound in air with temperature as a function of the other thermodynamic and physical quantities of influence These include: pressure, to account for the non-ideality of the gas; composition, mainly in consideration of the wide range variability of water vapor content; acoustic frequency, to define the impact of relaxation effects which give rise to dispersive sound propagation.

All these effects were previously considered by Zuckerwar for the development of a comprehensive predictive model of speed of sound in humid air[3] with a relative standard uncertainty on the order of 0.1%. In Sec. 2, we describe the formulation of this model and revise the uncertainty of its supporting parameters by updating the data sources for some relevant thermodynamic properties upon which the model is based, including the temperature dependence of the heat capacities and the virial coefficients of the main constituents of dry air and water vapor, by reference to equations of state, theoretical calculations, and correlations that recently became available. The critical revision of the input data and their combined contribution to the model leads to an estimated relative standard uncertainty as low as 25 ppm for the predicted speed of sound of humid air at ordinary, near-ambient, conditions of temperature, pressure, and humidity.

To support the validity of this claim with some experimental evidence, two different apparatus for speed of sound measurements were set up within a large-volume hemi-anechoic chamber available at Istituto Nazionale di Ricerca Metrologica (INRiM). Simultaneous measurements from the two experiments, sampling air in the same thermodynamic conditions, allowed us to verify the consistency of their results with the revised model predictions.

The first experiment, described in Sec. 3.1, is based on the measurement of the acoustic wavelength at fixed frequency f in the interval 16–22 kHz. The device measures the phase delay between a loudspeaker and a microphone where the distance between the two is changed under the precise control of a laser interferometer. This allows an accurate measurement of the wavelength λ leading to speed of sound w by the simplified relation $w = \lambda f$.

The second experiment, described in Sec. 3.2, employs a spherical microwave/acoustic resonator to measure speed of sound in batches of air continuously sampled from the chamber. The high quality factors of several purely radial acoustic modes allow for very precise acoustic measurements between 3 kHz and 20 kHz, which serve to test the modeled dispersion of speed of sound over the same frequency range. Also, the elevated accuracy that can be achieved using this instrument relies on the well-established physical model developed over the last 30 years for thermodynamic temperature measurements with monatomic gases.[4]

For both experiments, in Sec. 4 we present, analyze, and discuss the results obtained for a number of speed of sound measurements in humid air, with environmental parameters within the overall range 284 K < T < 301 K, 99.5 kPa < p <100 kPa, 30% < h_r < 60%, 400 ppm < x_{CO2} < 700 ppm. For a subset of these measurements, chosen to present simultaneous stable conditions of temperature in both experiments, we compare the results considering a detailed budget of their respective uncertainty. These results are further compared with the predictions of the model discussed in Sec. 2 and found to be consistent within their combined standard uncertainty.

The concluding remarks in Sec. 5 discuss the perspectives of future developments and applications of this work.

Finally, Sec. 6 presents software tools, in the form of both source and executable file made available for general use, to implement the model calculation of the speed of sound w as a function of the parameters of influence the production of plots and data tables, and the iterative calculation of the acoustic temperature from an experimental estimate of w.

2. Thermodynamic Model of Speed of Sound in Humid Air

2.1. Basic theory

The basic thermodynamic definition of the speed of sound w in gases is

$$w^2 = \left(\frac{\partial p}{\partial \rho}\right)_S, \tag{1}$$

where p is the pressure, ρ is the mass density, and the condition that the entropy S remains constant implies adiabatic, non-dispersive propagation of the sound wave. This leads to a simple expression for the squared speed of sound w_0 of an ideal gas, i.e., at zero pressure:

$$w_0{}^2(T) = \frac{\gamma_0 RT}{M}, \tag{2}$$

where $\gamma_0(T)$ is the ideal gas heat capacity ratio, T the thermodynamic temperature, R the molar gas constant, and M the molar mass of the gas. For a monatomic gas, γ_0 equals 5/3 independent of temperature, suggesting the acoustic determination of T can be used for accurate primary thermometry using gaseous He or Ar as the thermometric fluid[4]

Even at moderate atmospheric pressure, the deviations from ideality due to intermolecular forces become significant and must be accounted for to preserve the validity of the model

$$w^2(T,p) = \frac{\gamma_0 RT}{M}\left(1 + \beta_a p + \gamma_a p^2 + \cdots\right), \tag{3}$$

where the acoustic virial pressure coefficient $\beta_a(T)$, $\gamma_a(T)$, . . . are functions of only temperature, and the number of terms in Eq. (3) needed to preserve the accuracy of the model increases with increasing pressure. Each acoustic virial coefficient β_a, γ_a, . . . is related by a second-order differential equation to the corresponding density virial coefficient $B(T)$, $C(T)$, . . . of the virial equation of state

$$\frac{p}{\rho_n RT} = 1 + B\rho_n + C\rho_n{}^2 + \cdots, \tag{4}$$

where ρ_n is the molar density. For instance,

$$\beta_{\mathrm{a}} = \frac{1}{RT}\left[2B + 2(\gamma_0 - 1)T\frac{\mathrm{d}B}{\mathrm{d}T} + \frac{(\gamma_0 - 1)^2}{{\gamma_0}^2}T^2\frac{\mathrm{d}^2B}{\mathrm{d}T^2}\right], \tag{5}$$

so that the temperature dependence $\beta_{\mathrm{a}}(T)$ can be obtained by differentiation of $B(T)$, if this is independently known. We remark that the combination of Eqs. (3) and (5) also accounts for the pressure dependence of the heat capacities. Explicit expressions for the more complicated differential equation that relates $\gamma_{\mathrm{a}}(T)$ to $B(T)$ and $C(T)$ and their temperature derivatives, as well as complete definition of higher-order virials, can be found in Ref. 5.

For molecular gases, the statistical probability of excitation of rotational and vibrational degrees of freedom increases with temperature, making the heat capacities temperature-dependent. Also, in the presence of acoustic propagation at frequency f, the heat capacities become frequency-dependent due to relaxation, with the heat capacity ratio increasing for increasing frequency, making the speed of sound dispersive:

$$w^2(f) = w_{f=0}^2\left[1 + \frac{\varepsilon}{1-\varepsilon}\frac{(\omega\tau)^2}{1 + (\omega\tau)^2}\right], \tag{6}$$

where $\omega = 2\pi f$ is the angular frequency, $w_{f=0}$ is the speed of sound at zero frequency, and ε and τ are, respectively, the relaxation strength and the dispersion relaxation time. In Eq. (6), which strictly holds if a single relaxation process is active, the relaxation strength $\varepsilon(T)$, which depends only on temperature, measures the relative amplitude of the dispersive step

$$\varepsilon = 1 - w_{f=0}^2 / w_{f=\infty}^2, \tag{7}$$

with $w_{f=\infty}$ the high-frequency limit of the speed of sound, while the dispersion relaxation time $\tau(T,p)$ depends on temperature and pressure. Following Zuckerwar,[3] we keep the temperature and frequency dependence of the heat capacities separated, with each single relaxation process accounted for by a specific correction $K_{\mathrm{r}}(T, p, f)$ that depends on temperature, pressure, and frequency

$$K_{\mathrm{r}} = \frac{\varepsilon}{1-\varepsilon}\frac{(\omega\tau)^2}{1 + (\omega\tau)^2}. \tag{8}$$

With this organization, the squared speed of sound in a pure molecular gas can be expressed as:

$$w^2(T,p,f) = \frac{\gamma_0(T)RT}{M}\left(1 + \beta_{\mathrm{a}}(T)p + \gamma_{\mathrm{a}}(T)p^2 + \cdots\right) \times \left[1 + K_{\mathrm{r}}(T,p,f)\right]. \tag{9}$$

To be adequately representative of the speed of sound in humid air, i.e., a gaseous mixture with several components, the model summarized by Eq. (9) must properly account for the variable composition of the mixture. For simplicity, humid air will be considered as a binary mixture of water vapor and dry air, with respective mole fractions x_{w} and $x_{\mathrm{d}} = (1 - x_{\mathrm{w}})$. Hence, all thermodynamic quantities and relaxation parameters in Eq. (9) must be calculated as a function of x_{w} with appropriate mixing rules. Simple mole fraction weighted sums are appropriate for properties like molar mass and heat capacities, while density and acoustic virial coefficient require higher-order mixing rules that include the effect of water–air interaction virials. We note that for all these properties, these mixing rules are not empirical but refer to exact thermodynamic definitions Considering that relative humidity h_{r}, or the dew- or frost-point temperatures, are usually measured as experimental parameters instead of water mole fraction x_{w}, appropriate model equations are needed to convert between different humidity units and x_{w} that include an estimate of the temperature variation of the saturation pressure $p_{\mathrm{sat}}(T)$ of water and of the enhancement factor $f_{\mathrm{e}}(T, p)$ for the air–water system. For example, the conversion between relative humidity and water mole fraction is

$$x_{\mathrm{w}} = h_{\mathrm{r}} f_{\mathrm{e}}(T,p) p_{\mathrm{sat}}(T)/p. \tag{10}$$

Figure 1 presents an example of the complicated dependence of speed of sound in humid air from a particular combination of its influence parameters, namely f and x_{w}, as predicted by the model summarized by Eqs. (9) and (10). In this example, temperature, pressure, and $\mathrm{CO_2}$ concentration are respectively fixed at 293.15 K, 1 atm (0.101 325 MPa), and 368 ppm, and speed of sound is plotted at several acoustic frequencies between 100 Hz and 1 kHz as a function of relative humidity varying between 0% (dry air) and 12%. Two competing effects are visible, with speed of sound initially decreasing at low humidity as a consequence of relaxation, and then increasing at higher humidity due to a progressive increase of the ratio γ_0/M. The sensitivity of the location of the oxygen relaxation peak to slight variations of the concentration of water vapor in the mixture is evident by comparison of plots for different frequencies.

2.2. Thermodynamic model of speed of sound in humid air

In this section, we further discuss the theoretical grounds of our model calculation of speed of sound in humid air and the thermodynamic and relaxation data sources used to implement it,[6–49] which are summarized in Table 1.

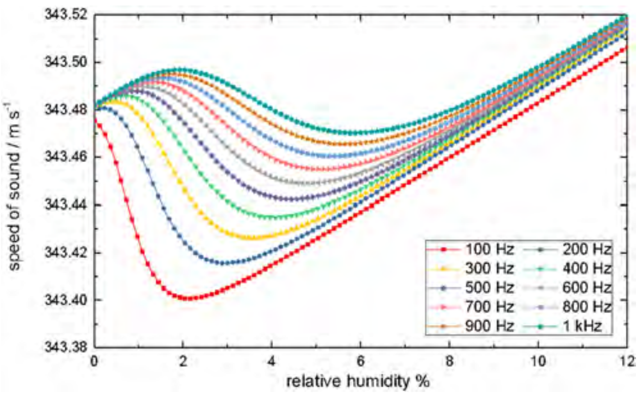

FIG. 1. Speed of sound in humid air at 293.15 K, 1 atm as a function of relative humidity at acoustic frequencies between 100 Hz and 1 kHz.

TABLE 1. Summary of thermodynamic data sources used to model speed of sound in humid air

Thermodynamic quantity – substance	Ref. data source	Temperature range of validity (K)	Notes	Additional ref. sources
		Molar mass		
Composition – dry air	*Standard atmosphere*[6] Picard *et al.*, CIPM 2007[8]		Adjusted for variable CO_2 content	Reference 7
Molar mass – dry air constituents, water	IUPAC[9,10]			Reference 11
		Ideal gas heat capacities		
Isobaric ideal gas heat capacity C_p^0 – nitrogen	Gamache and Orphanos[13]	1–9000		References 14–16
Isobaric ideal gas heat capacity C_p^0 – oxygen	Furtenbacher *et al.*[17]	1–5000	Corrected for updated values of fundamental constants and adjusted for isotopologues natural mixture[19]	
Isobaric ideal gas heat capacity C_p^0 – carbon dioxide	Tashkun and Harvey[20]	10–6000		Reference 21
Isobaric ideal gas heat capacity C_p^0 – methane	Setzmann and Wagner[22]	60–3000		
Isobaric ideal gas heat capacity C_{pw}^0 – water	Wagner and Pruß[23]	130–2000		
		Virial coefficient		
Second virial coefficient B_d – dry air	Zuckerwar[3]	230–647	*Square well* function fitted to experimental data and correlations[24–27] extrapolated down to 200 K	Reference 28
Second virial coefficient B_w – water	Harvey and Lemmon[31]	310–1170	Extrapolated down to 200 K	References 3, 23, and 32
Second interaction virial coefficient B_{dw} – air/water	Hellmann[33]	150–2000		Reference 34
Third virial coefficient C_d – dry air	Zuckerwar[3]	230–647	Empirical function fitted to experimental data and correlations[24,25,27] extrapolated down to 200 K	Reference 28
Third virial coefficient C_w – water	Zuckerwar[3]	473–1173	Empirical function fitted to experimental data[29] extrapolated down to 200 K	References 23 and 32
		Relaxation parameters		
Relaxation strengths and frequencies – nitrogen, oxygen	ANSI/ASA 51.26–2014 Standard[38] and Zuckerwar[3]	233–603	Extrapolated down to 200 K and up to 647 K	Reference 39
		Humidity conversion		
Saturation pressure p_{subl} over ice	Wagner *et al.*[45]	50–273.16		
Saturation pressure p_{sat} over water	Sonntag;[43] IAPWS[23]	173–373.16; 373.16–647		References 38 and 42
Enhancement factor – air–water system	Hyland[47]	193.15–363.15	Extended to 647 K using extrapolation methods discussed in Ref. 3	References 48 and 49

2.2.1. Molar mass of humid air

In our model, the molar mass of humid air M_a is defined by the mole fraction weighted sum of the molar mass of dry air M_d and that of water M_w

$$M_a = M_d(1 - x_w) + M_w x_w. \tag{11}$$

For the composition of dry air, we initially considered a list of 12 constituents, namely N_2, O_2, Ar, CO_2, Ne, He, Kr, CH_4, H_2, N_2O, CO, and Xe, with the corresponding molar fractions x_i defined and referred to as *Standard Atmosphere*,[6] assumed to be constant from sea level up to 80 km altitude. More recently, an accurate determination[7] of x_{Ar} was obtained, leading to revision of the reference CIPM 2007 formulation of the density of moist air.[8] The revision consequently affects, by subtraction, the concentration of all other species from unity,[7,8] including x_{N2}. Also, the concentrations of oxygen and carbon dioxide are fully correlated by combustion, photosynthesis, and respiration processes, being constrained to the constant sum $S = x_{O2} + x_{CO2} = 0.209\,79$. The uncertainties of x_{Ar}, x_{O2}, and x_{CO2}, discussed in Ref. 8, provide the most relevant contributions to the uncertainty of the molar mass of dry air, leading to the estimate $u_r(M_d) = 14.4$ ppm. For the minor constituents of dry air, different from N_2, O_2, Ar, CO_2, we retain the mole fractions originally defined in Ref. 6, but as reported in Ref. 3, where they are listed with more significant digits. Finally, we used the normalization given by Eq. (3) in Ref. 8 to account for the slight difference from unity of the total sum of the mole fractions of the constituents of dry air.

For the purpose of this work, the well-documented historical increase of CO_2 in the atmosphere, currently on the order of 20 ppm/decade, is particularly relevant, as an increase of the concentration of carbon dioxide x_{CO2} in air by 100 ppm decreases the speed of sound by 31 ppm. Hence, we found it convenient to implement our model calculation of speed of sound to account for an arbitrarily variable concentration x_{CO2} which, together with relative humidity, is a measured parameter in experimental work. Thus, both the molar mass of dry and humid air in Eq. (11) become dependent on CO_2 content, respectively as $M_d(x_{CO2})$ and $M_a(x_w, x_{CO2})$.

The value of the molar masses M_i of each constituent of dry air, and M_w for water, refer to the compilation of atomic weights and isotopic abundances maintained by the International Union of Pure and Applied Chemistry (IUPAC).[9–11] The natural variation of the isotopic abundances of the elements constituting air is sufficiently small to contribute negligible uncertainty to the calculation of M_a. In fact, even for the two major constituents, i.e., nitrogen and oxygen, the natural variation in atmospheric air is so small that their atomic weights are used as isotopic reference standards.[10] In contrast, the contribution of an imperfect estimate of the water vapor content to the uncertainty of M_a is not usually negligible. For example, if the relative humidity is determined with 1% uncertainty at ambient temperature and pressure, the corresponding contribution to the relative uncertainty of M_a is about 90 ppm.

For the molar mass of water, we adopt the value $M_w = 18.015\,28$ and the relative standard uncertainty $u_r(M_w) = 9.4$ ppm reported in Ref. 8, which is considered to be representative, by comparison with Refs. 9 and 10, of the H and O natural isotopic variation in seawater and continental water.

TABLE 2. Mole fractions, molar masses, and mass contributions of the constituents of dry air for a sample with CO_2 mole fraction of 500 ppm. Total molar mass of the resulting dry fraction M_d and humid air M_a for a sample of with $x_w = 0.05$

Constituent	Mole fraction	Molar mass (g mol^{-1})	Mass contribution (g mol^{-1})
Nitrogen	0.780 848	28.013 452	21.874 248
Oxygen	0.209 290	31.998 808	6.697 031
Argon	0.009 332	39.947 98	0.372 795
Carbon dioxide	0.000 500	44.010 01	0.022 005
Neon	1.818×10^{-5}	20.179 70	0.000 367
Helium	5.24×10^{-6}	4.002 602	0.000 021
Methane	2.00×10^{-6}	16.042 43	0.000 032
Krypton	1.14×10^{-6}	83.798 00	0.000 096
Hydrogen	5.0×10^{-7}	2.015 970	0.000 001
Nitrous oxide	2.7×10^{-7}	44.013 06	0.000 012
Carbon monoxide	1.9×10^{-7}	28.010 09	0.000 005
Xenon	8.7×10^{-8}	131.2930	0.000 011
Total mass of dry air $M_d = 28.966\,69$ g mol^{-1}			
Water		18.015 28	
Total mass of humid air with $x_w = 0.05$, $M_a = 28.419\,12$ g mol^{-1}			

As a summarizing example, Table 2 lists the molar fractions, the molar masses, and the corresponding mass contributions for the constituents of a sample of dry air with $x_{CO2} = 0.0005$ (500 ppm). Also listed in Table 2 is the total mass of the dry fraction M_d and the resulting total mass of humid air M_a in the presence of water vapor with concentration $x_w = 0.05$.

2.2.2. Ideal gas heat capacities of humid air

The ideal gas heat capacity ratio $\gamma_0(T)$, which appears as a multiplying factor in the right-hand side of Eq. (9), decreases with

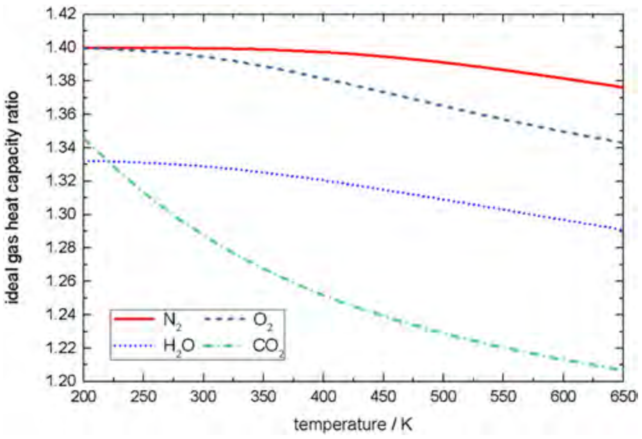

FIG. 2. Ideal gas heat capacity ratio of major molecular constituents of humid air as a function of temperature.

increasing temperature (see Fig. 2) because of the increasing excitation of the vibrational modes associated with several molecular constituents of humid air, namely N_2, O_2, H_2O, and CO_2, with variable impact on the speed of sound depending on their concentration.

For the calculation of $\gamma_0(T)$, we use the standard thermodynamic relation

$$\gamma_0(T) = 1 + \left[\left(C_p^0(T)/R\right) - 1\right]^{-1}, \tag{12}$$

where the molar isobaric ideal gas heat capacity of humid air $C_p^0(T)$ is defined by the separate contributions of dry air $C_{pd}^0(T)$ and water vapor $C_{pw}^0(T)$

$$C_p^0 = C_{pd}^0(1 - x_w) + C_{pw}^0 x_w. \tag{13}$$

The left plot in Fig. 3 shows that, at constant temperature, the ideal gas heat capacity ratio defined by Eqs. (12) and (13) decreases with increasing humidity; this is because of the smaller γ_0 of water compared to molecular nitrogen and oxygen. Conversely, the ratio γ_0/M, which enters in the definition of the speed of sound as a multiplying factor, increases as a function of increasing humidity (see right plot in Fig. 3), because the decrease of M for increasing water vapor content is a stronger effect than the decrease of γ_0.

Because of the large sensitivity of the speed of sound to heat capacity, the choice of accurate reference sources for the evaluation of $C_{pd}^0(T)$ and $C_{pw}^0(T)$ is particularly important. In the original formulation of the model by Zuckerwar,[3] the choice was made to refer to the cubic polynomial interpolations of $C_{pd}^0(T)$ and $C_{pw}^0(T)$ reported in Ref. 12, for dry air and water vapor respectively, which were based on a selection of spectroscopic, molecular structure, and thermodynamic data available by 1970. The relative standard uncertainty of the heat capacities attributed in Ref. 3 to these interpolations was 0.5% for dry air and 1% for water vapor for the overall temperature range between 250 K and 1500 K, resulting in the largest contribution to the overall uncertainty of the speed of sound modeled in Ref. 3.

In order to revise and reduce this uncertainty contribution, we found it more convenient to address the calculation of the ideal gas heat capacity by a separate estimate for each major constituent of air. For the whole dry fraction, the weighted sum

$$\frac{C_{pd}^0}{R} = \sum_i \left(\frac{C_{pi}^0}{R}\right) x_i \tag{14}$$

is calculated for the list of i constituents and molar fractions x_i specified in Table 2, upon correcting x_i depending on CO_2 concentration which is an arbitrarily variable parameter of our speed of sound model.

For the isobaric heat capacity of molecular nitrogen, the prevalent constituent of the dry air mixture, we assume its calculation from the total partition sum of $^{14}N_2$ and its isotopologues recently obtained in Ref. 13 over the wide range between 1 K and 9000 K. The results of this calculation favorably compare with a previous model[14] and, over the limited temperature range where they are available, with experimental determinations based on speed of sound measurements in nitrogen.[15,16]

For the isobaric heat capacity of molecular oxygen, we assume the results of its calculation between 1 K and 5000 K from a recent comprehensive analysis of spectroscopic data.[17] These results, initially obtained only for $^{16}O_2$, were successively corrected using updated values of the fundamental constants[18] and adjusted to include the isotopologues of natural oxygen, leading to a slight revision of their values and the associated uncertainties.[19]

In this context, the extremely low uncertainty of the heat capacity of nitrogen and oxygen, respectively less than 0.2 ppm and 5 ppm between 200 K and 600 K, as estimated in Ref. 13 and in Refs. 17 and 19, drastically reduces their contribution to the speed of sound uncertainty (see Sec. 2.3).

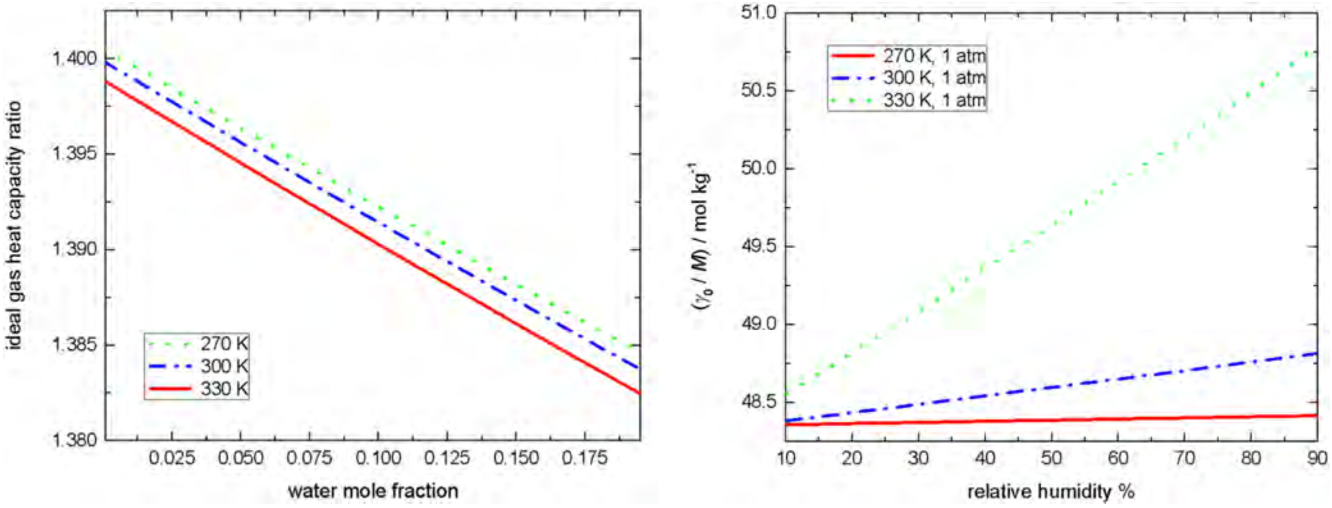

FIG. 3. (Left plot) Ideal gas heat capacity ratio γ_0 of humid air at 270, 300, and 330 K as a function of water molar fraction x_w. (Right plot) Ratio γ_0/M of humid air at 270, 300, and 330 K as a function of relative humidity.

In comparison to N_2 and O_2, the weighted contribution of minor molecular constituents to the overall heat capacity of dry air is small, due to their low concentration. For the temperature dependence of the ideal heat capacity of CO_2, we refer to its recent, extremely accurate, calculation,[20] fitted as a continuous function of temperature with relative uncertainty on the order of a few ppm, in Ref. 21. For the ideal heat capacity of CH_4, we assume its revised model equation[22] with relative uncertainty less than 0.1%.

The normalized ideal gas isobaric heat capacity C_p^0/R of the monatomic constituents of air, namely Ar, He, Ne, and Kr, is assumed to be exactly 5/2 and independent of temperature.

Finally, for the temperature dependence of the isobaric heat capacity of the water molecule C_{pw}^0 we assume its estimate from Eq. (5.6) in Ref. 23, where several statistical mechanical models based on spectroscopic data are critically revised and compared. Over the limited range between 200 K and 600 K, which is of interest in this work, we conservatively estimate the standard relative uncertainty of $C_{pw}^0(T)$ to be 0.1%, upon considering the difference between the reference equation and various data sources, as compared in Ref. 23.

2.2.3. Virial coefficients of humid air

Our model of the second virial coefficient of humid air B accounts for the separate contributions of dry air B_d and water vapor B_w using the appropriate binary mixing rule

$$B = B_d(1 - x_w)^2 + 2B_{dw}(1 - x_w)x_w + B_w {x_w}^2, \tag{15}$$

where B_{dw} is the air–water interaction coefficient.

For the temperature dependence of B_d, we use the functional form

$$B_d = a_d - b_d \exp(c_d/T), \tag{16}$$

motivated by the assumption of a square-well intermolecular potential energy function. The parameters in Eq. (16), namely $a_d = 152.2$ cm^3 mol^{-1}, $b_d = 111.3$ cm^3 mol^{-1}, $c_d = 108.1$ K, obtained in Ref. 3 by fitting to various data compilations,[24–27] provide a definition of B_d that differs from the alternative estimate of B_d from a thermodynamic property formulation for *standard* dry air[28] by -0.4 cm^3 mol^{-1} at 200 K and -1 cm^3 mol^{-1} at 647 K. This difference is accounted for with a specific uncertainty contribution discussed in Sec. 2.3.

For the temperature dependence of the second virial coefficient of water vapor B_w, we compared predictions from the following sources: (i) a function of the same form of Eq. (16) evaluated in Ref. 3 from the B_w data collected in Ref. 29, supposed valid between 420 K and 1170 K; (ii) the IAPWS 1995 equation,[23] as implemented in reference database software;[30] (iii) a recent correlation function by Harvey and Lemmon,[31] based on a critical review of experimental data, with stated validity between 310 K and 1170 K; (iv) fully quantum calculations from flexible-monomer *ab initio* potentials,[32] reported between 200 K and 2000 K. From this comparison, it is evident that, even within its range of validity, the difference of the "square-well" function[3,29] from other sources is significantly larger (by a factor of 6 at 420 K) than its standard uncertainty estimate in Ref. 3. Above 310 K, the correlations and calculations[23,31,32] of B_w are all found in extremely good agreement, with maximum relative differences of ±5% between 310 K and 647 K from their average and from the most accurate experimental data. At lower temperatures, B_w becomes rapidly more negative (see left plot in Fig. 4) and a realistic uncertainty estimate of the correlations,[23,31] which need to be extrapolated below their original range of validity, is harder to assess. Taking the *ab initio* calculation from the CCpol-8sf potential[32] as a baseline for comparison below 310 K, maximum relative differences of 20% and 35% are found at 200 K for the correlating function,[31] which is extrapolated below its stated range of validity, and a "square-well" fit[23] respectively. In spite of these large differences, the resulting impact on the calculated value of the second density virial of humid air B, and hence on the speed of sound, is usually limited by the small concentration of water vapor at low temperature (see right plot in Fig. 4). Thus, we found it convenient to assume the correlation function[31] as our reference source for the calculation of B_w over the full temperature range between 200 K and 647 K, accounting for the difference from alternative estimates[23,32] of B_w with a specific uncertainty contribution discussed in Sec. 2.3.

Figure 4 shows that, over the entire temperature range, the air–water interaction virial coefficient B_{dw} is much smaller in magnitude than the corresponding B_w, making its contribution to B very small. Based on this observation, the approach in Ref. 3 was to simply ignore the interaction coefficient. The contribution of B_{dw}, however, is not negligible in the context of the accuracy aimed for in the present work. For example, at 293.15 K and 1 atm, with 50% relative humidity corresponding to $x_w = 0.0116$, neglecting B_{dw} in the definition of B would impact the calculated speed of sound in humid air with a relative change of 30 ppm. For the temperature dependence of B_{dw}, we relied on the most recent and accurate first principles calculation by Hellmann.[33] Comparison with a previous calculation of B_{dw} by Harvey and Huang[34] shows excellent agreement, with differences below 1 cm^3 mol^{-1} over the entire range between 150 K and 2000 K.

To extend the range of validity of our model of the speed of sound to moderately high pressures, on the order of 10 MPa, an additional term must be considered in the virial Eq. (4), i.e., the third virial coefficient C of humid air, rigorously defined as

$$\begin{aligned} C = {} & C_d(1 - x_w)^3 + 3C_{ddw}(1 - x_w)^2 x_w \\ & + 3C_{wwd}(1 - x_w){x_w}^2 + C_w {x_w}^3, \end{aligned} \tag{17}$$

where C_d is the third virial coefficient of dry air, C_w is the third virial coefficient of water, and the two terms C_{ddw} and C_{wwd} account for three-body cross interactions air–air–water and air–water–water, respectively.

Following the approach in Ref. 3, we define the temperature dependence of the third density virial C_d of dry air by a suitable modification of the *square well* function defined in Eq. (16),

$$C_d = [d_d - e_d \exp(f_d/T)] \exp(g_d/T) + C_{\infty d}, \tag{18}$$

where the parameters $d_d = 3871$ cm^6 mol^{-2}, $e_d = 1237$ cm^6 mol^{-2}, $f_d = 171.1$ K, $g_d = 0.0058$ K^{-1}, and $C_{\infty d} = 1000$ cm^6 mol^{-2} were obtained[3] by fitting to various data and correlations.[24,25,27] The alternative estimate of C_d from the thermodynamic property formulation for *standard* dry air[28] differs from the prediction of Eq. (18) by 980 cm^6 mol^{-2} at 200 K and 400 cm^6 mol^{-2} at 647 K. This difference is accounted for with the specific uncertainty contribution described in Sec. 2.3.

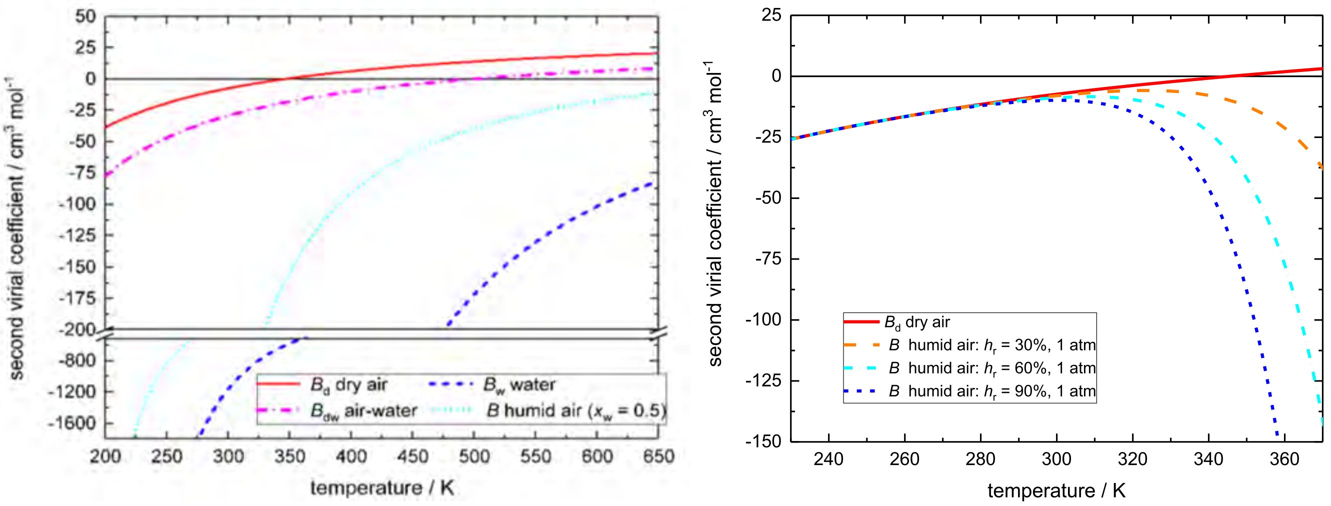

FIG. 4. (Left plot) Comparison of the second virial coefficient of dry air B_d, water vapor B_w, humid air B with $x_w = 0.5$, and second interaction virial of the air–water system B_{dw} between 380 K and 600 K. (Right plot) Second virial coefficient of humid air B at different relative humidity, atmospheric pressure.

For the temperature dependence of the third virial coefficient of water vapor C_w, we compared predicted estimates from three alternative sources: (i) the IAPWS-95 equation[23] as implemented in Ref. 30; (ii) the fit reported in Ref. 3, in the form of Eq. (18), to a selection of experimental data from Ref. 29 supposed valid down to 423 K, requiring extrapolation at lower temperatures; (iii) the first principles calculations[32] available for a few selected temperatures between 300 K and 1000 K, whose predicted estimates vary considerably depending on the particular type of assumed intermolecular potential. Above 400 K, all these sources are found in reasonable agreement with differences which are commensurate to the stated uncertainties and the dispersion of experimental data. At lower temperature, the rapid increase of the magnitude of C_w which becomes exponentially more negative, and the few experimental data available (only above 373 K) more subject to absorption errors and generally less accurate, make it challenging to evaluate a realistic uncertainty estimate for the extrapolated estimates from Ref. 23 or from Refs. 3 and 29. Finally, we choose to estimate C_w by the same functional form of Eq. (18) with the parameters determined in Ref. 3, namely d_w = 39 540.1 cm^6 mol^{-2}, e_w = 124.38 cm^6 mol^{-2}, f_w = 3595.3 K, g_w = 0.0043 K^{-1}, $C_{\infty w}$ = 200.3 cm^6 mol^{-2}. Extrapolation of this function down to 200 K entails a large uncertainty accounted for by a specific contribution discussed in Sec. 2.3. However, in this temperature range the uncertainty contribution of C_w to the calculated speed of sound is limited by the extremely low partial pressure of water vapor in the mixture.

Fitted functions for the third interaction virial coefficient C_{ddw} and C_{wwd} are available[35] based on previous theoretical estimates.[36,37] However, these functions are characterized by large uncertainty, on the order of 100% and 200% for C_{ddw} and C_{wwd}, respectively, and do not fully cover the temperature range of interest for our model. We therefore prefer to assume C_{ddw} and C_{wwd} equal to zero, which reduces Eq. (17) to

$$C = C_d(1 - x_w)^3 + C_w x_w{}^3, \tag{19}$$

accounting for the different alternative definition of C from Eq. (17) instead of Eq. (19) in our estimate of the standard uncertainty of C discussed below in Sec. 2.3.

The temperature derivatives of the density virial coefficients which are needed to determine the corresponding acoustic virial coefficients as in Eq. (5), were calculated analytically or numerically, depending on the type of reference data source available for the former. Differentiation was implemented separately for the individual contributions of dry air, water, and the air–water interaction virial, and the resulting functions combined using appropriate mixing rules to calculate the resulting acoustic virials of humid air. For instance, the second acoustic virial pressure coefficient of humid air β_a is defined as

$$\beta_a = \beta_d(1 - x_w)^2 + 2\beta_{dw}(1 - x_w)x_w + \beta_w x_w{}^2, \tag{20}$$

where

$$\beta_d = \frac{1}{RT}\left[2B_d + 2(\gamma_{0d} - 1)T\frac{dB_d}{dT} + \frac{(\gamma_{0d} - 1)^2}{\gamma_{0d}}T^2\frac{d^2B_d}{dT^2}\right], \tag{21}$$

$$\beta_w = \frac{1}{RT}\left[2B_w + 2(\gamma_{0w} - 1)T\frac{dB_w}{dT} + \frac{(\gamma_{0w} - 1)^2}{\gamma_{0w}}T^2\frac{d^2B_w}{dT^2}\right], \tag{22}$$

$$\beta_{dw} = \frac{1}{RT}\left[2B_{dw} + 2(\gamma_{0dw} - 1)T\frac{dB_{dw}}{dT} + \frac{(\gamma_{0dw} - 1)^2}{\gamma_{0dw}}T^2\frac{d^2B_{dw}}{dT^2}\right], \tag{23}$$

and γ_{0d}, γ_{0w}, and γ_{0dw} are, respectively, the ideal gas heat capacity ratios of dry air, water, and humid air.

With modification from the equations reported in Ref. 3, required by the inclusion of the interaction coefficient B_{dw} in Eq. (15), the third acoustic pressure virial coefficient of humid air γ_a is defined as

$$\gamma_a = \frac{\left[L_{Bd}(1-x_w)^2 + 2L_{Bdw}(1-x_w)x_w + L_{Bw}{x_w}^2\right]^2(\gamma_0-1)/\gamma_0 + L_{Cd}(1-x_w)^3 + L_{Cw}{x_w}^3}{(RT)^2} - \frac{B\beta_a}{RT}, \tag{24}$$

where B and β_a are the second density and acoustic pressure virial coefficient of the humid air mixture, respectively defined by Eqs. (15) and (20), and, as for the definition of C in Eq. (19), third virial cross-interaction terms are ignored. In Eq. (24), the terms L_{Bd}, L_{Bw}, and L_{Bdw} correspond to second acoustic density virial coefficients respectively defined as

$$L_{Bd} = B_d + (2\gamma_{0d}-1)T\frac{dB_d}{dT} + (\gamma_{0d}-1)T\frac{d^2B_d}{dT^2}, \tag{25}$$

$$L_{Bw} = B_w + (2\gamma_{0w}-1)T\frac{dB_w}{dT} + (\gamma_{0w}-1)T\frac{d^2B_w}{dT^2}, \tag{26}$$

$$L_{Bdw} = B_{dw} + (2\gamma_{0dw}-1)T\frac{dB_{dw}}{dT} + (\gamma_{0dw}-1)T\frac{d^2B_{dw}}{dT^2}, \tag{27}$$

and the terms L_{Cd}, and L_{Cw} correspond to third acoustic density virial coefficients respectively defined as

$$L_{Cd} = \frac{(1+2\gamma_{0d})}{\gamma_{0d}}C_d + \frac{({\gamma_{0d}}^2-1)}{\gamma_{0d}}T\frac{dC_d}{dT} + \frac{(\gamma_{0d}-1)^2}{2\gamma_{0d}}T^2\frac{d^2C_d}{dT^2}, \tag{28}$$

$$L_{Cw} = \frac{(1+2\gamma_{0w})}{\gamma_{0w}}C_w + \frac{({\gamma_{0w}}^2-1)}{\gamma_{0w}}T\frac{dC_w}{dT} + \frac{(\gamma_{0w}-1)^2}{2\gamma_{0w}}T^2\frac{d^2C_w}{dT^2}. \tag{29}$$

Following Eq. (3), the combination of the second and third acoustic virial pressure coefficient define the virial correction K_v

$$K_v(T,p) = \beta_a(T)p + \gamma_a(T)p^2, \tag{30}$$

which determines the pressure dependence of the squared speed of sound as a function of temperature. The left plot in Fig. 5 shows the second and third acoustic virial pressure coefficient of dry air over a temperature range that encompasses their zero-crossing temperatures, respectively around 250 K for β_a and 160 K for γ_a. Below 160 K, both β_a and γ_a are negative and the speed of sound monotonically decreases for increasing pressure; between 160 K and 250 K, β_a is negative and γ_a is positive, resulting in the speed of sound first decreasing with pressure, reaching a minimum, and then increasing. Above 250 K, the speed of sound monotonically increases with pressure. These alternative pressure trends are shown in the right plot in Fig. 5.

2.2.4. Relaxation parameters

The speed of sound dispersion induced by a single relaxation process, as described by Eqs. (6)–(8), is not representative of the complexity of relaxation phenomena in humid air, which involve several vibrational-vibrational and vibrational-translational energy exchanges among four constituents, namely N_2, O_2, H_2O, and CO_2, with nitrogen and oxygen mainly responsible for absorption, and the frequency location of their dispersion steps being sensitively affected by humidity (see Fig. 6).

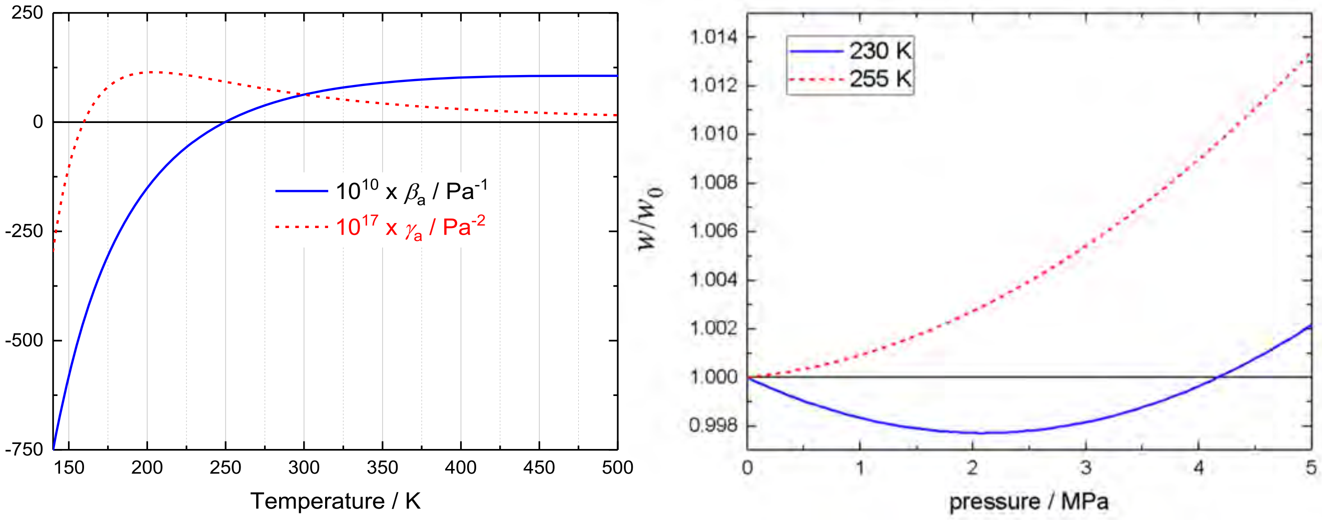

FIG. 5. (Left) Second β_a and third γ_a acoustic virial pressure coefficient of dry air, respectively showing zero-crossing temperature around 250 and 160 K. (Right) Ratio w/w_0 of speed of sound in dry air to its zero-pressure value for two temperatures: at 230 K the second acoustic virial pressure coefficient β_a is negative while the third γ_a is positive resulting in a minimum of w around 2 MPa; at 255 K both acoustic virials are positive resulting in a monotonic increasing trend of w. (Right) Ratio w/w_0 of speed of sound in dry air to its zero-pressure value for two temperatures

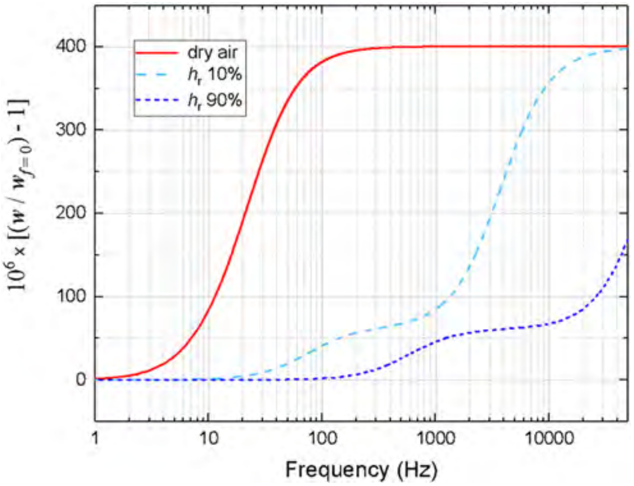

FIG. 6. Relative difference of the ratio between the speed of sound in humid air *w* and its limiting value $w_{f=0}$ at zero frequency for three different humidity conditions at 293.15 K, 1 atm. For dry air, the relaxation frequencies of nitrogen and oxygen fall near 9 and 24 Hz merging in a single dispersion step; for increasing relative humidity, the dispersion steps of nitrogen and oxygen progressively separate by orders of magnitude, appearing well resolved respectively at lower and higher frequencies.

Because a description of relaxation effects is of interest to calculate acoustic attenuation caused by sound absorption in the atmosphere, available absorption and dispersion data have been subject to extensive study, resulting in a standard correlation[38] which defines the density and humidity dependence of the relaxation frequencies of molecular nitrogen and oxygen and the temperature dependence of their relaxation strengths as thoroughly discussed in Ref. 3, and briefly summarized below. Not being aware of any recent experimental determination of the relaxation parameters of the constituents of air which might improve this description, we assume its validity between 200 K and 647 K, which slightly extends the temperature range considered in Ref. 3, and implement it in our model as such. Basically, relaxation frequencies are defined in Refs. 3 and 38 instead of relaxation times.

For nitrogen, the relaxation frequency f_{N2}

$$f_{N2} = p^* \left(\frac{T_{ref}}{T}\right)^{0.5} [a_{N2}(T) + b_{N2}(T) x_w], \tag{31}$$

is a function of pressure p^* in atm, temperature in K, and water mole fraction x_w, with $T_{ref} = 293.15$ K. At T_{ref}, $a_{N2} = 9$ Hz and $b_{N2} = 28$ kHz. Otherwise, the temperature dependence $a_{N2}(T)$ and $b_{N2}(T)$ is defined[3] as

$$a_{N2}(T) = 6.614 \times 10^4 \exp\left(-58.90 T^{-1/3}\right), \tag{32}$$

$$b_{N2}(T) = 2.8 \times 10^4 \exp\left\{-4.17\left[(T/T_{ref})^{-1/3} - 1\right]\right\}. \tag{33}$$

For oxygen, the relaxation frequency f_{O2}

$$f_{O2} = p^* \left[a_{O2}(T) + b_{O2} x_w \frac{c_{O2}(T) + x_w}{d_{O2} + x_w}\right], \tag{34}$$

is a function of pressure p^* in atm, temperature in K, and water mole fraction x_w. At 293.15 K, $a_{O2} = 24$ Hz, $b_{O2} = 4.04$ MHz, $c_{O2} = 2 \times 10^{-4}$, $d_{O2} = 3.91 \times 10^{-3}$. The temperature dependence of $a_{O2}(T)$ and $c_{O2}(T)$, which becomes significant at high temperatures, was first determined by Bass[39] and is defined[3] as

$$a_{O2}(T) = 2.131 \times 10^5 \exp\left(-60.40 T^{-1/3}\right), \tag{35}$$

$$c_{O2}(T) = 16.46 \exp\left(-75.19 T^{-1/3}\right). \tag{36}$$

The relaxation strengths of nitrogen ε_{N2} and oxygen ε_{O2} are respectively defined as

$$\varepsilon_{N2} = \frac{x_{N2} C_{N2} R}{C_p^\infty (C_p^0 - R)}, \tag{37}$$

and

$$\varepsilon_{O2} = \frac{x_{O2} C_{O2} R}{C_p^\infty (C_p^0 - R)}, \tag{38}$$

where C_p^0 is the heat capacity of humid air defined in Eq. (13) and C_p^∞ its limiting value at high frequency

$$C_p^\infty = C_p^0 - x_{N2} C_{N2} - x_{O2} C_{O2}, \tag{39}$$

where x_{N2} and x_{O2} are corrected proportionally to the dry air fraction $(1 - x_w)$ and C_{N2} and C_{O2}, defined[3] as

$$C_{N2} = R\left(\frac{3352.0}{T}\right)^2 \frac{\exp(-3352.0/T)}{[1 - \exp(-3352.0/T)]^2}, \tag{40}$$

$$C_{O2} = R\left(\frac{2239.1}{T}\right)^2 \frac{\exp(-2239.1/T)}{[1 - \exp(-2339.1/T)]^2}, \tag{41}$$

account for the temperature dependence of the vibrational heat capacities of nitrogen and oxygen. Finally, a suitable expression of the relaxation correction K_r of the humid air mixture is

$$K_r = \frac{\varepsilon_{N2}}{1 - \varepsilon_{N2}}\left[\frac{(f/f_{N2})^2}{1 + (f/f_{N2})^2}\right] + \frac{\varepsilon_{O2}}{1 - \varepsilon_{O2}}\left[\frac{(f/f_{O2})^2}{1 + (f/f_{O2})^2}\right], \tag{42}$$

which simultaneously accounts for the progressive inaccessibility (*freezing*) of vibrational degrees of freedom at high frequency and their progressive activation for increasing temperature.

2.2.5. Humidity

As mentioned above, in most experimental determinations of speed of sound in air the water vapor content x_w is not measured directly, though this would be possible in principle, for example by microwave hygrometry[40,41] with the spherical resonator used in this work. Instead, relative humidity h_r or the dew- or frost-point temperature are usually measured using various type of hygrometers, with the conversion to x_w of these alternative humidity units requiring predictive equations for two functions, namely the saturation pressure of pure water $p_{sat}(T)$ or, below 273.16 K, the sublimation pressure of ice $p_{subl}(T)$, which are functions of temperature only, and a correcting function $f_e(T, p)$, which depends on temperature and pressure, usually referred to as the enhancement factor, used to correct p_{sat} and p_{subl} for vapor nonideality and the effect of added pressure.

Several alternative sources for the calculation of p_{sat} and p_{subl} are available in the form of tabulated correlations or equations.[38,42–45] In spite of being mostly based on the same original experimental data, some of these alternatives became of more common use among different communities, including those active in meteorology, hygrometry, and in the measurement and modeling of thermophysical properties. The reference equations for p_{sat} have also been historically updated to account for changes of the International Temperature Scale or refine estimates of specific thermodynamic states, like the pressure of the triple point of water.

Following the critical evaluation of some of these alternatives, the choice was previously made in Ref. 3 to adopt the saturation pressure equation reported in the ANSI standard,[38] assumed to be valid between 233 K and 603 K. However, a limit of this choice is that below 273.16 K, the ANSI equation only estimates the saturation pressure over (supercooled) water rather then the sublimation pressure over ice, which may be a case of practical interest for some applications. More versatile are the equations first proposed by Sonntag,[43] revised in Ref. 46, which are of widespread use in hygrometry, covering the range between 173 K and 373 K and offering two different series of coefficients for saturation over water or over ice. More recently, a reference equation for the sublimation pressure of ice p_{subl} became available,[45] which is preferable for the estimate of p_{subl} between 200 K and 273.16 K because of its low uncertainty.

Below 373 K, the relative difference between p_{sat} predicted by the Sonntag equation and the auxiliary equation[42] considered in the formulation of the IAPWS reference equation of water[23] is always less than ±0.01%, well within the stated uncertainty of the IAPWS formulation. Above 373 K, the relative difference between p_{sat} as predicted by IAPWS or Sonntag rapidly increases up to 12% at 647 K, showing that the latter cannot be usefully extrapolated in this range.

All things considered, in the present work we choose to use the reference equation[45] for the calculation of p_{subl} between 200 K and 273.16 K, adopt the Sonntag equation[43,46] for the prediction of p_{sat} between 200 K and 373.16 K, and the IAPWS equation[42] for the prediction of p_{sat} above 373.16 K up to 647 K.

Interpolating equations for the enhancement factor of the air–water system all derive from the seminal work of Hyland,[47] which reports tabulated estimates of $f_e(T, p)$ covering the temperature range from 193.15–363.15 K and the pressure range from 25 kPa to 10 MPa. Over the restricted pressure range up to 2 MPa, Greenspan equations[48] offer a simpler tool for the computation of f_e with distinct sets of coefficients for air over water or over ice in the temperature range between −50 °C and 0 °C; more recent work[49] updates the coefficients of Greenspan equations from IPTS-68 to ITS-90.

In order to model speed of sound over temperature and pressure ranges as wide as possible, we interpolated the sets of coefficients[3] listed in Table 3 as a function of pressure to define the temperature dependence of f_e by the polynomial equation

$$\ln(f_e) = a_e + b_e/T + c_e/T^2. \tag{43}$$

Equation (43) and the coefficients in Table 3 were obtained in Ref. 3 by fitting Hyland's original data between 233.15 K and 363.15 K along selected isobars between 0.5 atm and 100 atm; the fitted functions have then been extrapolated to higher temperatures (up to 600 K) with the constraint that $f_e = 1$ at $1/T = 0$, based on the observation that in the limit of infinite temperature the air–water mixture must approach ideality.

TABLE 3. Coefficients of Eq. (43) for the natural logarithm of the enhancement factor f_e along selected isobars

Pressure (atm)	a_e	b_e	c_e
0.5	−0.001 02	0.350 3	136.34
1	−0.002 01	0.844 6	231.06
2	0.012 72	−1.922 12	217.09
5	0.056 85	−25.640 9	4 177.29
10	0.076 99	−37.988 0	7 372.09
20	0.094 74	−51.216 5	12 330.9
50	0.119 44	−78.128 9	26 101.4
100	0.223 72	−163.300 2	55 803.2

2.3. Overall model uncertainty and comparison with previous correlations and measurements

In Table 4, for different conditions of temperature, pressure, humidity, and frequency, we list some comparative examples of the uncertainty contribution of various sources, namely ideal gas heat capacities, virial coefficients, relaxation parameters, humidity unit conversion, and molar mass, to the overall uncertainty of our model calculation of the speed of sound in humid air. The combined uncertainty from these contributions, obtained from their quadrature sum, is also listed in the rightmost column of Table 4. The estimate of each of these individual contributions is motivated and discussed in the remainder of this section.

Looking at the list of thermodynamic and acoustic conditions considered in Table 4, it is evident that the range of interest for the majority of applications, with pressure lower than 1 atm, temperature in the range between −40 °C and 60 °C, acoustic frequency within a few tens of kHz, and arbitrarily variable humidity, the overall relative standard uncertainty of our modeled speed of sound in humid air is always less than 50 ppm. We remark that the 0.1% overall uncertainty estimate previously reported by Zuckerwar,[3] with a prevalent contribution from the heat capacity correction based on reference data,[12] considering the progress made in the calculation of thermodynamic properties and the development of dedicated equations of state (EoS) for the main constituents of air and water, appears indeed outdated and far too conservative.

The uncertainty of the molar mass of air, discussed in Sec. 2.2.1, has contributions from the molar mass of the dry fraction $u_r(M_d)$ = 14.4 ppm and the molar mass of water $u_r(M_w)$ = 9.4 ppm. Its contribution to the overall uncertainty of the speed of sound in humid air $u_r(w)$, on the order of 6–8 ppm, is only slightly variable depending on the concentration of water vapor x_w.

Following the notation used in Ref. 3, and to facilitate the comparison with tabulated speed of sound and uncertainties reported there, we rewrite Eq. (9) as

$$w^2(T,p,f) = \frac{\gamma_s RT}{M}[1 + K_c(T)][1 + K_v(T,p)][1 + K_r(T,p,f)]. \tag{44}$$

TABLE 4. Examples of uncertainty budgets for the model calculation of speed of sound in humid air

Environmental, composition, and acoustic parameters[a]							Relative corrections and uncertainty contributions to speed of sound calculation					
Temperature (K)	Temperature (°C)	Pressure (atm)	Relative humidity (%)	Water mole fraction x_w	Frequency (kHz)	Speed of sound (m/s)	$K_c/2$ Heat capacity correction (ppm)	$K_v/2$ Virial correction (ppm)	$K_r/2$ Relaxation correction (ppm)	Estimate of water mole fraction (ppm)	Molar mass (ppm)	Combined relative standard uncertainty (ppm)
293.15	20	1	0	0	0	343.3333 ± 0.0079	−509.4 ± 0.1	293.4 ± 21.9	0	0	7.2	23.1
293.15	20	10	0	0	0	344.3427 ± 0.1092	−509.4 ± 0.1	3240 ± 317	0	0	7.2	317
293.15	20	0.5	0	0	0	343.2826 ± 0.0044	−509.4 ± 0.1	145.8 ± 10.7	0	0	7.2	12.9
293.15	20	1	50	0.011 584	0	343.9578 ± 0.0081	−525.9 ± 2.4	271.3 ± 22.4	0	0.8	7.2	23.6
293.15	20	1	0	0	10	343.4708 ± 0.0079	−509.4 ± 0.1	293.4 ± 21.9	398.8 ± 0.0	0	7.2	23.1
293.15	20	1	0	0	0.1	343.4643 ± 0.0099	−509.4 ± 0.1	293.4 ± 21.9	380.0 ± 17.5	0	7.2	29.0
293.15	20	1	50	0.011 584	10	343.9875 ± 0.0083	−525.9 ± 2.4	271.3 ± 22.4	86.4 ± 4.5	0.8	7.2	24.0
293.15	20	1	50	0.011 584	0.1	343.9596 ± 0.0081	−525.9 ± 2.4	271.3 ± 22.4	5.1 ± 1.4	0.8	7.2	23.7
233.15	−40	1	50	0.000 094	10	306.1809 ± 0.0109	−160.4 ± 0.1	−175.3 ± 34.8	79.4 ± 0.0	0.0	7.2	35.5
273.15	0	1	50	0.003 029	10	331.6548 ± 0.0092	−356.1 ± 0.7	181.0 ± 25.6	198.4 ± 8.0	0.2	7.2	27.8
303.15	30	1	50	0.021 027	10	350.3069 ± 0.0085	−639.2 ± 4.3	291.9 ± 21.3	91.2 ± 1.5	7.8	7.1	24.2
333.15	60	1	50	0.098 691	10	371.7209 ± 0.0176	−1184 ± 19	132.2 ± 23.3	158.9 ± 4.2	35.3	7.0	47.2
373.15	100	1	50	0.501 422	10	422.3728 ± 0.0462	−2954 ± 89	−2349 ± 61	57.0 ± 12.8	10.9	5.9	109
423.15	150	5	50	0.479 232	10	445.8364 ± 0.1050	−4548 ± 85	−4895 ± 216	6.4 ± 1.9	43	6.0	236
473.15	200	10	25	0.395 186	10	464.2390 ± 0.1348	−6152 ± 70	−1777 ± 277	4.4 ± 1.3	53	6.2	290
573.15	300	50	15	0.270 689	10	505.4705 ± 0.5633	−9711 ± 48	14 955 ± 1110	0.8 ± 0.3	90	6.5	1114
623.15	350	100	5	0.090 630	10	526.7073 ± 1.4604	−10 772 ± 17	48 998 ± 2773	2.9 ± 0.9	40	7.0	2773

[a] All the entries in Table 4 are calculated for a sample of humid air whose composition is adjusted to include a CO_2 mole fraction of 500 ppm.

In Eq. (44), the temperature-dependent heat capacity correction term K_c, defined as

$$K_c(T) = [\gamma_0(T)/\gamma_s] - 1, \tag{45}$$

accounts for the relative difference between the ideal heat capacity ratio γ_0 of a sample of humid air and its temperature-independent corresponding γ_s calculated for a sample with the same composition under the assumption that rotational degrees of freedom are fully excited and vibrational degrees of freedom are fully unexcited. Differentiating the definition of K_c, we obtain the sensitivity of this correction with respect to a small change of C_p^0.

$$\frac{\Delta K_c}{1 + K_c} = u_r(\gamma_0) = -u_r\left(C_p^0\right)(\gamma_0 - 1). \tag{46}$$

Interestingly, Eq. (46) shows that the relative uncertainty of the correction $u_r(K_c)$ is always less in magnitude than the relative uncertainty of the heat capacity, because $(\gamma_0 - 1)$ is always less than unity.

Our estimate of the overall relative uncertainty of the heat capacity of humid air $u_r(C_p^0)$ is obtained by the weighted sum of the relative uncertainties of the heat capacities of the mixture components, using their molar fractions as weights and the individual contributions discussed in Sec. 2.2.1. Between 200 K and 647 K, these are almost negligible for both nitrogen and oxygen, respectively less than 0.2 ppm and 5 ppm, and thus for dry air (see Table 4), due to the remarkable progress achieved in the calculation of fundamental molecular properties.[13,17] A larger contribution is given by the uncertainty of the heat capacity of water vapor. For instance, Table 4 considers a sample of air that has 500 ppm of CO_2, with 50% relative humidity at 293.15 K and 1 atm, corresponding to a water mole fraction of 1.16%. The resulting estimate of $u_r(C_p^0)$ is 12.2 ppm, mainly due to the contribution of $C_{p\mathrm{w}}^0$. The corresponding relative uncertainty contribution to the squared speed of sound from the ideal heat capacity ratio is then $u_r(w^2) = u_r(\gamma_0) = u_r(C_p^0)\ (\gamma_0 - 1)$, about 5 ppm in the preceding example, finally contributing only 2.4 ppm to the combined relative standard uncertainty $u_r(w)$ of the speed of sound. At constant relative humidity, this contribution increases at high temperature due to the increasing saturation pressure of water.

To determine the sensitivity of the acoustic virial correction $K_v(T, p)$, previously defined by Eq. (30), to the uncertainty of the virial coefficients of humid air B and C, the starting point is an estimate of the standard uncertainty of the density virials of dry air B_d and C_d, water B_w and C_w, and water–air interaction B_{dw} from the comparison of alternative data sources and correlations available for these properties, discussed in Sec. 2.2.3. As pointed out in Ref. 3, we recall that it is not meaningful to specify relative uncertainty estimates for quantities like the virial coefficients that may change sign over the temperature range of interest.

For the uncertainty of the second density virial of dry air, we assume $u(B_d) = 0.35 + 2.5 \times 10^{-3}\ |T/\mathrm{K} - 375|\ \mathrm{cm^3\ mol^{-1}}$ which accounts for the difference of the estimate of B_d from Eq. (16) or the formulation for *standard* dry air.[28] Over the range 200–647 K, this difference varies between a minimum of 0.3 $\mathrm{cm^3\ mol^{-1}}$ at 375 K and a maximum of 0.95 $\mathrm{cm^3\ mol^{-1}}$ at 647 K. It is worth noting that for small concentration of water vapor, i.e., in most ordinary conditions of humid air near ambient temperature and pressure, the contribution of $u(B_d)$ to the overall uncertainty of the modeled speed of sound is dominant. For the second density virial of water, upon considering the differences between the chosen estimate of B_w from the correlation function[31] from two alternatives,[23,32] as well as the dispersion of the most accurate existing experimental data supporting these estimates, we assume the decreasing exponential function $u(B_w) = 2.95 + 1.84 \times 10^7 \exp(-T/23.75\ \mathrm{K})\ \mathrm{cm^3\ mol^{-1}}$, which varies between 4000 $\mathrm{cm^3\ mol^{-1}}$ at 200 K and 3 $\mathrm{cm^3\ mol^{-1}}$ at 647 K, to be conservatively representative of the uncertainty of B_w. For the second air–water interaction virial coefficient B_{dw}, we assume the standard uncertainty estimate of its calculation,[33] which varies between a maximum of 1.6 $\mathrm{cm^3\ mol^{-1}}$ at 200 K to a minimum of 1 $\mathrm{cm^3\ mol^{-1}}$ at 647 K.

Our estimate of the standard uncertainty of the third virial coefficient of dry air $u(C_d)$ accounts for the different prediction of C_d between two alternatives[3,28] discussed in Sec. 2.2.3. The difference increases exponentially with decreasing temperature between 647 K and 200 K and is well represented as $u(C_d) = 408 + 1.45 \times 10^4 \exp(-T/61.2\ \mathrm{K})\ \mathrm{cm^6\ mol^{-2}}$, which is considerably larger than the constant $u(C_d) = 220\ \mathrm{cm^6\ mol^{-2}}$ previously assumed in Ref. 3 to be representative over the entire temperature range. For the third density virial coefficient of water vapor C_w, the comparison of alternative estimates[3,23,32] leads us to assume $u(C_w) = 1500 + 0.5|C_w|\ \mathrm{cm^6\ mol^{-2}}$ which, particularly at temperatures below 400 K, appears more realistic than the previous estimate $u(C_w) = 86 + 0.25|C_w|\ \mathrm{cm^6\ mol^{-2}}$ in Ref. 3.

Finally, the absolute uncertainty of the virial coefficients of humid air is obtained from the combination of those of dry air and water using the appropriate mixing rules, respectively for the second density virial B

$$u(B) = u(B_d)(1 - x_w)^2 + 2u(B_{dw})(1 - x_w)x_w + u(B_w){x_w}^2, \tag{47}$$

and for the third density virial C

$$u(C) = u(C_d)(1 - x_w)^3 + u(C_w){x_w}^3, \tag{48}$$

where, as discussed in Sec. 2.2.3, the third-order cross-interaction coefficients are neglected.

Explicit analytic expressions for the sensitivity $\Delta K_v/(1 + K_v)$ of the virial correction to small changes of the second and third density virial coefficients of humid air and, therefrom, through their temperature derivatives, from the corresponding acoustic virial coefficients β_a and γ_a, can be found in Refs. 3 and 50, and are not reported here for the sake of brevity. In addition to the definition of $u(B)$ and $u(C)$ by Eqs. (47) and (48), these expressions require the temperature dependence of the ideal gas heat capacity ratio $\gamma_0(T)$ from Eq. (12), of the second acoustic virial coefficient $\beta_a(T)$ from Eq. (20), and differentiable forms of the density virials $B(T)$ and $C(T)$; in Ref. 3 the latter are analytically obtained from *square well* functions like Eqs. (16) and (18). Additionally, all these supporting parameters must be properly weighted to account for the composition of the air–water binary mixture. Some comparative examples of the contribution $0.5\Delta K_v/(1 + K_v)$ to the relative standard uncertainty of the speed of sound in humid air $u_r(w)$ for different conditions of temperature, pressure, and humidity are illustrated in Fig. 7 and listed in Table 4. Because K_v accounts for the non-ideality of the gas, its contribution generally increases at high density, i.e., at lower temperature and larger pressure.

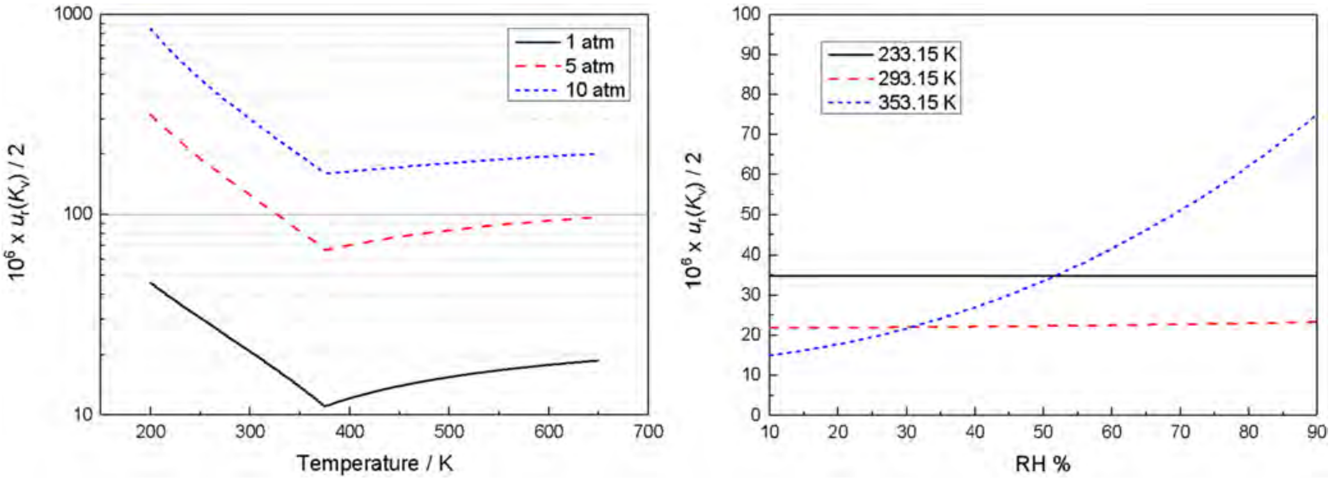

FIG. 7. Relative contribution of the virial correction $0.5\Delta K_v/(1 + K_v)$ in ppm to the uncertainty of the speed of sound. (Left) for dry air, as a function of temperature between 200 K and 647 K for three different pressures, namely 1, 5, 10 atm. (Right) For humid air at 1 atm, as a function of relative humidity, for three different temperatures, namely 233.15, 293.15, 353.15 K.

The uncertainty of the relaxation correction $K_r(T, p, f)$, defined by Eq. (42), has contributions from the relaxation frequencies and the relaxation strengths of nitrogen and oxygen; however, because the latter are defined by the corresponding temperature dependence of the heat capacities, and thus very accurately known compared to the relaxation frequencies, their uncertainty contribution can be neglected. Based on Ref. 51, the relative standard uncertainties of the relaxation frequency of nitrogen and oxygen are assumed respectively: $u_r(f_{N2})$ = 15% for $f_{N2} \geq 200$ Hz and f_{N2} = 25% below 200 Hz; $u_r(f_{O2})$ = 10% for $f_{O2} \geq 30$ Hz and $u_r(f_{O2})$ = 50% below 30 Hz. In terms of these assumptions, an expression for the sensitivity $\Delta K_r/(1 + K_r)$ of the relaxation correction to the uncertainty of the relaxation frequencies is determined in Ref. 3 as

$$\frac{\Delta K_r}{1+K_r} = \frac{-2f^2}{1+K_r}\left[\frac{\varepsilon_{N2}}{1-\varepsilon_{N2}}\frac{f_{N2}^2 u_r(f_{N2})}{\left(f_{N2}^2+f^2\right)^2} + \frac{\varepsilon_{O2}}{1-\varepsilon_{O2}}\frac{f_{O2}^2 u_r(f_{O2})}{\left(f_{O2}^2+f^2\right)^2}\right]. \tag{49}$$

The uncertainty of the relaxation correction is often a minor contribution to the speed of sound uncertainty budget, except for those cases when the frequency happens to coincide with the dispersion step of nitrogen and/or oxygen, which sensitively depend on humidity (see Fig. 5). For example, for a sample of dry air at 293.15 K and 1 atm the relaxation correction defined by Eq. (42) amounts to (380 ± 18) ppm at 100 Hz and to (399.000 ± 0.004) ppm at 10 kHz. At the same temperature and pressure, for a sample of humid air with 50% relative humidity the relaxation correction becomes (5.1 ± 1.4) ppm at 100 Hz and (86.4 ± 4.5) ppm at 10 kHz. At high temperatures, where the water saturation pressure becomes significant allowing for water–air mixtures where the molar fraction of water predominates, the relaxation frequencies of nitrogen and oxygen increase by orders of magnitude, making negligible both the relaxation correction and the associated uncertainty (see Table 4).

Because the water vapor content of humid air is not usually known in terms of molar fraction, the conversion from relative humidity or dew-point temperature to x_w brings additional uncertainty to the modeled speed of sound, with contributions from the saturation pressures p_{sat} and p_{subl}, and from the enhancement factor f_e. Considering first the uncertainty of p_{sat} and p_{subl}, because these properties are defined by different equations (see Sec. 2.2.5) over different temperature ranges, we assume the following: $u_r(p_{subl})$, varying between 0.2% at 200 K and 5.5×10^{-6} at 273.16 K, from the corresponding estimate of $U_r(p_{subl})$ by Eq. (5a) in Ref. 45; for supercooled water, from 200 to 273.16 K, $u_r(p_{sat})$ = [0.01 − 0.005(T − 273.15 K)]%, from a revision of the original Sonntag[43] estimate given by Eq. (22) in Ref. 46; from 273.16 to 373.16 K $u_r(p_{sat})$ = 0.005% from the original Sonntag[43] estimate in this range; above 373.16 K, $u_r(p_{sat})$ = 0.025% from the IAPWS formulation.[23,42]

As for the uncertainty of the enhancement factor, it becomes more significant at low temperature and high pressure. Our chosen source[3] for the calculation of f_e considers contributions to $u_r(f_e)$ from the original Hyland data[47] and the quality of the fitted interpolation of those, with the former spanning between a minimum relative uncertainty of 10 ppm for f_e = 1.0039 at 363.15 K and 100 kPa and a maximum of 7.5% for f_e = 1.88 at 223.15 K, 10 MPa. However, the relative difference between the predictive functions in Ref. 3 and the data in Ref. 47 significantly exceeds the estimate of $u_r(f_e)$ proposed in Ref. 3. This discrepancy becomes particularly relevant (one order of magnitude) above ambient temperature at ordinary (near ambient) pressure, the reason being that, contrary to the form of the fitting functions used in Ref. 3, Hyland's estimates of f_e do not monotonically decrease as a function of increasing temperature along isobars. While further investigation of this anomaly is outside the scope of this work, we augmented the estimate of $u_r(f_e)$ proposed in Ref. 3 to account for the discrepancies. We thus assume the following, with p in kPa: for $T \leq 293.15$ K, $u_r(f_e) = p[1 - 5 \times 10^{-2}(T - 363.15)] \times 10^{-6}$, as originally in Ref. 3; for 293.15 K < T

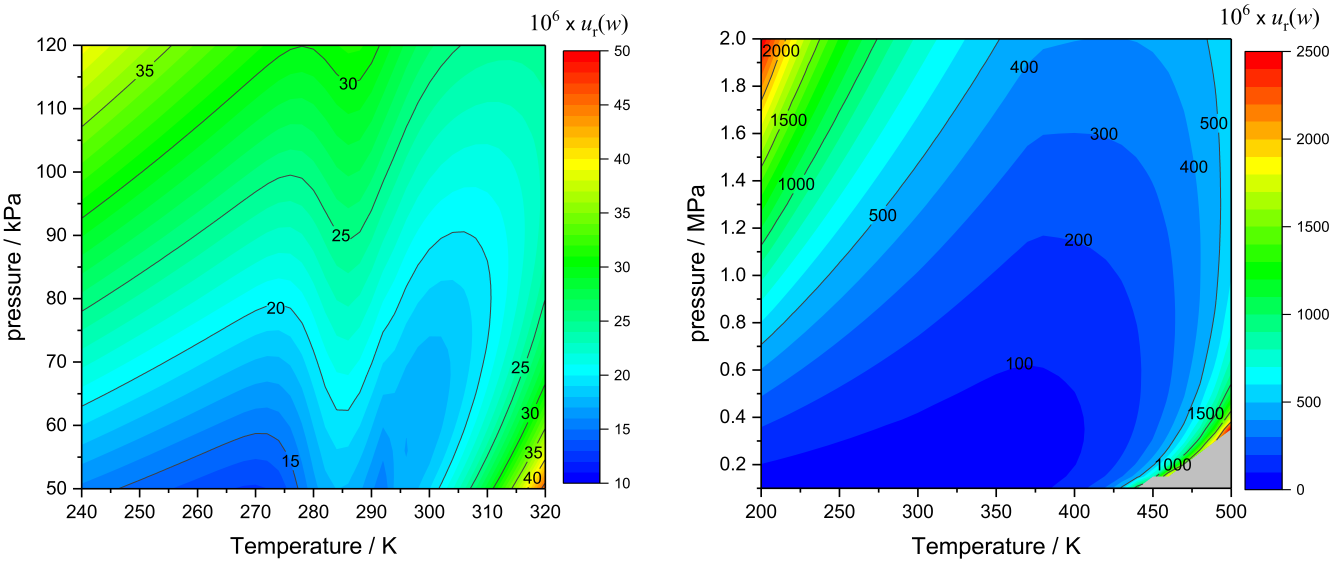

FIG. 8. Relative standard uncertainty of modeled speed of sound in humid air, $u_r(w)$, as a function of temperature and pressure for a sample of air with h_r = 30%, x_{CO2} = 500 ppm, f = 10 kHz. (Left) near-ambient conditions, 240 K ≤ T ≤ 320 K, 50 kPa ≤ p ≤ 120 kPa. (Right) extended range, 200 K ≤ T ≤ 500 K, 100 kPa ≤ p ≤ 2 MPa.

≤ 363.15 K, $u_r(f_e) = 0.2/p + p[1 - 5 \times 10^{-2}(T - 363.15)] \times 10^{-6}$, modified to account for the discrepancies discussed above; for 363.15 K $< T \le 603.15$ K, $u_r(f_e) = p[0.5 - 2.08 \times 10^{-3}(T - 603.15)] \times 10^{-6}$, different from $u_r(f_e) = 0$ proposed in Ref. 3 which appears unrealistic at elevated pressures.

Considering that a rigorous analytical propagation of the uncertainty of x_w onto the speed of sound of humid air would be greatly complicated by the dependence upon x_w of all the thermophysical properties included in the acoustic model, to resolve such complication, we evaluated the uncertainty contribution to the speed of sound w as $0.5|w(x_w + u(x_w)) - w(x_w - u(x_w))|$ by repeated software implementation of the model. At near-ambient conditions of temperature and pressure, this contribution is typically within a few ppm, though it rapidly increases in

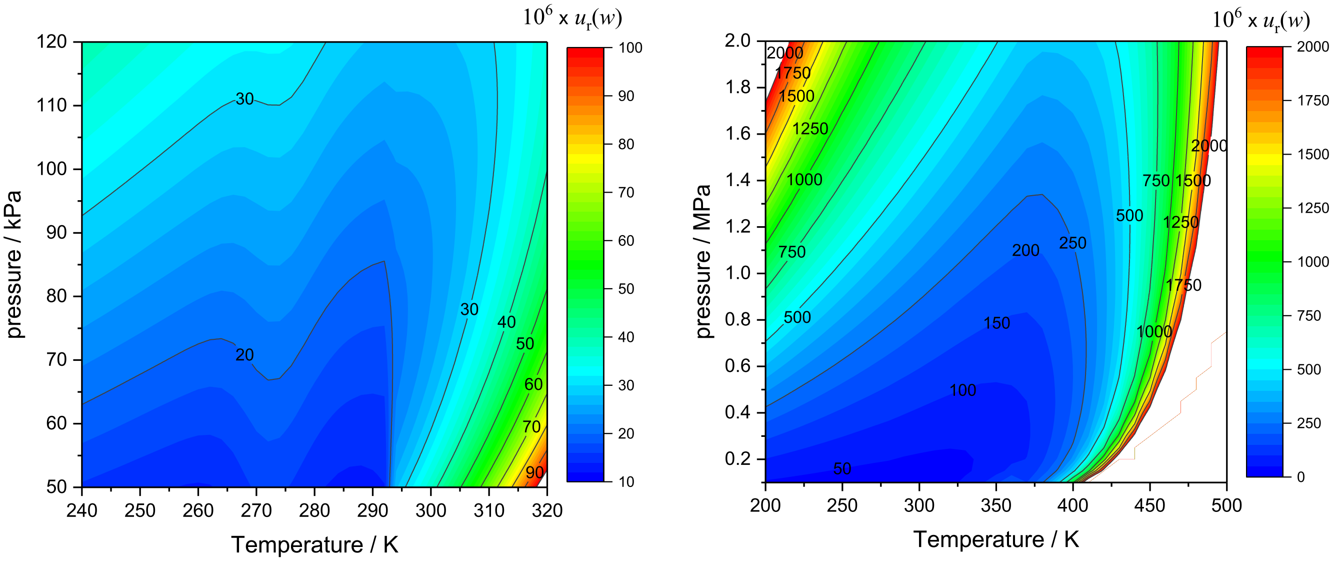

FIG. 9. Relative standard uncertainty of modeled speed of sound in humid air, $u_r(w)$, as a function of temperature and pressure for a sample of air with h_r = 70%, x_{CO2} = 500 ppm, f = 10 kHz. (Left) near-ambient conditions, 240 K ≤ T ≤ 320 K, 50 kPa ≤ p ≤ 120 kPa. (Right) extended range, 200 K ≤ T ≤ 500 K, 100 kPa ≤ p ≤ 2 MPa; white areas correspond to values of $u_r(w)$ exceeding 2000 ppm, and/or combinations p, T resulting in water mole fractions x_w exceeding unity.

TABLE 5. Comparison of different model calculations of speed of sound in humid air

Environmental, composition, and acoustic parameters[a]								
Temperature (K)	Temperature (°C)	Pressure (atm)	Relative humidity (%)	Water mole fraction x_w	Frequency (kHz)	Speed of sound this work (m/s)	Speed of sound Zuckerwar model[3] (m/s)	Speed of sound Cramer model[52] (m/s)
273.15	0	1	40	0.002 423	0	331.5682 ± 0.0088	331.59 ± 0.33	331.575 ± 0.099
293.15	20	1	60	0.013 901	0	344.0945 ± 0.0082	344.11 ± 0.34	344.115 ± 0.103
303.15	30	1	80	0.033 642	0	350.9820 ± 0.0098	351.00 ± 0.39	351.008 ± 0.105
233.15	−40	2	60	0.000 057	20	306.1384 ± 0.0229	306.14 ± 0.34	NA
293.15	20	10	40	0.000 955	50	344.5357 ± 0.1091	344.54 ± 0.45	
323.15	50	1	80	0.097 805	10	366.0778 ± 0.0181	366.09 ± 0.40	
373.15	100	5	80	0.163 079	20	397.5038 ± 0.0488	397.44 ± 0.48	
373.15	100	0.5	40	0.801 462	20	451.6195 ± 0.0668	451.44 ± 0.81	
523.15	250	10	12	0.485 880	100	495.9468 ± 0.1468	496.09 ± 1.84	
603.15	330	50	16	0.431 901	20	528.6747 ± 0.6549	526.86 ± 2.63	

[a] All the entries in Table 5 are calculated for a sample of humid air whose composition is adjusted to include a CO_2 mole fraction of 368 ppm.

proportion to the increase of x_w, e.g., for large relative humidity at high temperature.

For different relative humidities, respectively 30% and 70%, Figs. 8 and 9 outline the variation of the relative standard uncertainty of the modeled speed of sound $u_r(w)$ in humid air, as a function of temperature and pressure, between 200 K and 500 K and from 50 kPa to 2 MPa.

All things considered, the reduction of the overall uncertainty achieved by the present update of the speed of sound model first worked out in Ref. 3 is indeed significant, spanning between factors of 4 and 40, depending on the thermodynamic condition.

It should be stressed that this achievement relies on improved estimates of the heat capacities and the virial coefficients of the main constituents of air and water obtained over the last 40 years. Assuming that these new estimates are based on well critically assessed theoretical and experimental work increases our confidence in the accuracy of the model. To reinforce this confidence, as discussed in the following sections, we tested the validity of the speed of sound model by comparison with the results obtained by two different experiments. Such comparison is relevant within the limited range of environmental conditions that were accessible and within the limited accuracy of the experiments. As discussed in the concluding section, validation over wider ranges of conditions will require more experimental tests in well-controlled laboratory conditions.

Before the publication of the Zuckerwar model,[3] a calculation of the speed of sound in air as a function of temperature, pressure, humidity, and CO_2 concentration had been proposed by Cramer.[52] Though the validity of Cramer's model is limited to temperatures between 0 °C and 30 °C, pressures between 76 kPa and 102 kPa, water and CO_2 mole fractions respectively up to 0.06 and 0.01, the low overall uncertainty, estimated to be on the order of 300 ppm, and its practical availability in the form of a simply implementable interpolating equation make it still widely used in all fields of acoustics and beyond.

It is of some interest to compare the predictions of the model of speed of sound in humid air presented in this work with the original model published by Zuckerwar[3] and with Cramer's interpolating equation,[52] upon setting the calculations for the fixed mole fraction x_{CO2} = 368 ppm assumed in Ref. 3. Table 5 lists the results of this comparison for some selected temperature, pressure, and humidity values. Comparison with the predictions of Cramer are limited to zero acoustic frequency, as speed of sound dispersion was not considered in his model. Remarkably, all the predictions of the model elaborated in the present work are found consistent with those calculated from Refs. 3 and 52 within the combined standard uncertainties. Particularly, at ordinary conditions of temperature (233 K $< T <$ 373 K), pressure ($p <$ 10 atm), and humidity ($x_w <$ 0.2), the relative difference between this work and the Zuckerwar model[3] is always less than 120 ppm. The remarkable quality of the agreement supports the initial motivation for this work, i.e., that the uncertainty estimate of 0.1% for speed of sound in humid air by Zuckerwar[3] was far too conservative. At less ordinary conditions of temperature (T > 373 K), pressure (p > 10 atm), and for mixtures particularly rich in water content (0.2 $< x_w <$ 1), the relative difference between this work and the Zuckerwar model[3] rapidly increases up to the order of 0.1%, because of the different reference equation chosen for water saturation pressure assumed here.

It is also interesting to compare the predictions of the model presented in this work with previous experimental determinations of the speed of sound in air. Among the many that appeared in the past literature, a subset of seven articles published between 1919 and 1963 was selected in Ref. 3 as being better documented with regard to the description of the experimental method and the preparation of the sample. Many of those works report an estimate of speed of sound w_{STP} in dry air at *standard* conditions (T = 273.15 K, p = 1 atm) at zero frequency, providing a reference for comparison. The most accurate reported such determination[53] provides w_{STP} = (331.45 ± 0.01) m s^{-1} for a sample with x_{CO2} = 300 ppm, which favorably compares to w_{STP} = (331.448 ± 0.008) m s^{-1} predicted by the model presented in this work.

More recently, measurements of the speed of sound in air were obtained[54] using a spherical resonator at 255 K for pressures up to 6.9 MPa, in the frequency range between 6 kHz and 30 kHz. These results are extremely accurate, with $u_r(w)$ = 10 ppm, though they lack an estimate of residual water vapor content and CO_2 molar fraction, and resulted in agreement within 250 ppm with two models of thermodynamic properties of air. Remarkably, the results tabulated in Ref. 54 are consistent, within their combined uncertainties, with the predictions of the model presented here. For example, at 255 K and 6.88 MPa, the highest pressure explored in Ref. 54, the reported estimate of 329.475 m s^{-1} is consistent with our prediction w = (328.0 ± 3.1) m s^{-1}; at 255 K and 30.81 kPa, the reported estimate[54] of 320.269 m s^{-1} is consistent with our prediction w = (320.272 ± 0.004) m s^{-1}, assuming x_{CO2} = 350 ppm as a plausible estimate for the air sample used in Ref. 54.

3. Experimental Determinations of Speed of Sound

A comprehensive review of experimental methods for measuring speed of sound and absorption in fluids is outside the scope of this work and can be found elsewhere.[55] All these methods basically fall in two main categories, namely transient methods, which determine speed of sound from measurement of the propagation time of an acoustic signal over a known distance, and steady-state methods, which depend on the determination of some characteristic parameter of standing waves formed within a reflecting enclosure with fixed or variable dimensions. To the former category belong most of the methods used for the first historically documented speed of sound measurements[56] and, still today, for acoustic thermometry applied to length interferometry,[57] or in acoustic-based distance meters[58] (e.g., parking sensors, echography, or sonar), and for accurate determinations of speed of sound in liquids and gases at high pressures,[59,60] i.e., fluids whose characteristic acoustic impedance does not differ enough from that of a solid boundary to provide efficient reflection. While transient methods can be extremely precise, they are not well suited for measurements in a dispersive fluid like humid air at atmospheric pressure. Ideally, the propagating sound signal (e.g., a burst) should be as short as possible to better define its start and arrival times. However, the shorter the signal the wider its harmonic content and, since both attenuation and the speed of the sound strongly depend on frequency, the sound pulse may suffer significant distortion, complicating correlation of the generated and detected signals. Additionally, it is difficult to define the starting and the arrival points of the signal, because of the finite non-negligible dimensions of both the source and the detector. In conclusion, dispersion limits the accurate measurement of time, while the dimension of the source and receiver limits the accuracy of the measurement of distance. The acoustic wavelength meter, dubbed λ-meter for brevity, described in Sec. 3.1, implements a steady-state method designed to overcome both limitations: dispersion is avoided by generating a constant-frequency continuous wave, the indefiniteness of the distance is eliminated by the possibility to vary the distance between source and receiver by an amount that is accurately measurable with the aid of an optical technique. A second steady-state method implemented in this work, described in Sec. 3.2, is based on a fixed-volume resonant cavity spherical geometry. The resonator determines speed of sound by the combination of acoustic and microwave resonance frequency measurements, with the latter providing information on the internal dimensions of the cavity using speed of light as an exact reference. This technique relies on the accurate modeling of various types of perturbations and the definition of appropriate corrections first achieved by Moldover, Mehl and co-workers,[61,62] which lead to the most accurate speed of sound measurements to date, and is now widely used for the realization of acoustic primary temperature standards.[4] The two experimental methods implemented in this work for speed of sound measurements in air are thus based on significantly different working principles and techniques, enhancing the meaningfulness of the comparison of the experimental results with the predictions of the model discussed above.

The two experiments were prepared for simultaneous operation in a large acoustic test chamber (floor surface 110 m^2, internal volume 450 m^3) set up in a hemi-anechoic configuration. This setting was chosen to minimize the possible influence of diffraction, whose perturbing effects on the λ-meter are difficult to model *a priori*. Differently from interferometric techniques, which are originally designed to operate in large open environments or outdoors, acoustic resonators are usually employed in laboratory conditions, with temperature, pressure, and sample composition under extremely accurate control. Bench-setup of the resonator inevitably impairs the practical operation of the instrument, due to delay in reacting to rapid changes of environmental parameters, primarily temperature.

With the aim of cross-checking the results obtained from the two experiments, they were mounted within the chamber at a small distance from each other, at approximately the same elevation from the floor where air temperature, pressure, relative humidity, and CO_2 concentration were measured (see Fig. 10).

Two sets of 100 Ω industrial platinum resistance thermometers (IPRTs) were used in the experiments. The first set is comprised of six IPRTs (Model SE 012), deployed along the acoustic path of the λ-meter. These thermometers were calibrated at INRiM with an expanded uncertainty (coverage factor k = 2) of 0.01 K in the range 0–30 °C. The IPRTs resistance is measured using a Fluke 1586A Super-DAQ system, which fully preserves the accuracy of the

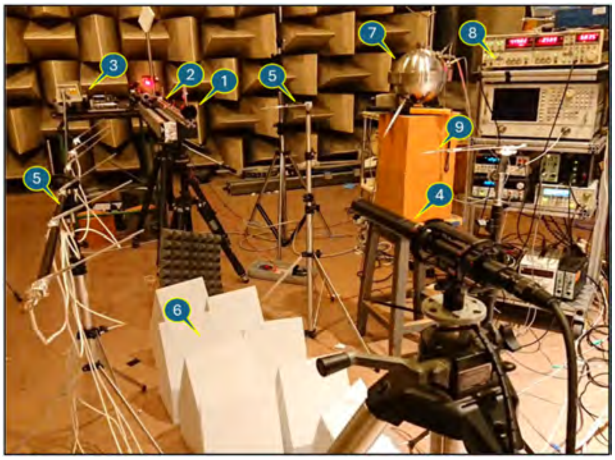

FIG. 10. Experimental setup in a hemi-anechoic chamber for comparison of speed of sound measurements in air with an acoustic wavelength meter and a spherical acoustic resonator. At the background/left is visible the loudspeaker (1) mounted on the moving carriage (2) under the control of an interferometer (3). At the foreground on the right is visible the microphone on the tripod (4). At the left the array of resistance thermometers (5). On the floor foam absorbers for reducing acoustic reflections (6). Top right the spherical resonator (7) with the related electronic bench (8). A hygrometer and a pressure sensor (9), together with a CO_2 sensor, complete the environmental parameters measurement.

calibration. The second set is comprised of four IPRTs, with two additionally deployed on the acoustic path of the λ-meter and the other two inserted in the bosses at the top and the bottom ends of the resonator. These thermometers were also calibrated at INRiM, with an expanded uncertainty of 0.01 K in the range 0–30 °C, but in this case the calibration accuracy could not be fully exploited due to the relatively less accurate instrumentation used to measure the resistance of the thermometers, a 6.5 digits multimeter (Keithley 2000), which finally sets the standard uncertainty of our measurements of air temperature in the chamber, and within the resonator, at 0.025 K, yet still sufficient for comparisons of the speed of sound measurements with the model.

The atmospheric air pressure in the chamber was measured using a Druck DPI 142 barometer with 0.01% uncertainty, as declared by the manufacturer, which spans beyond the need of the present work. The carbon dioxide mole fraction x_{CO2} and the relative humidity of air were measured by a single handheld instrument (Testo 440) equipped with a combined $\mathrm{CO_2}$-sensing and thermo-hygrometric probe (Testo 0632.1552). The probe measures x_{CO2} up to 0.1% with standard uncertainty on the order of 80 ppm, and relative humidity in the range 5%–95% with relative standard uncertainty of about 2%. These specifications set a lower limit to the overall uncertainty of our experimental determinations of speed of sound in air with relative contributions of about 25 ppm and 80 ppm from our imperfect estimates of x_{CO2} and h_{r}, respectively.

While the thermostatting system of the chamber allowed for coarse temperature control within the range 10–50 °C, temperature readings on the two experiments seldom were sufficiently stable and consistent at the level needed for a meaningful cross comparison of the two experiments. For this reason, we therefore examine and discuss the results of a limited subset of the complete measurement campaign conducted in the chamber, with emphasis on results obtained near 294 K at atmospheric pressure. A larger acoustic measurement subset was available for the wavelength meter experiment which was more rapidly responsive to variations of ambient conditions in the chamber. Anticipating the detailed discussion of these comparisons in Sec. 4 below, we remark that the agreement between the experiments and the model was satisfactory over the entire explored range of temperature, humidity, and $\mathrm{CO_2}$ concentration.

3.1. Acoustic wavelength-meter

3.1.1. Working principle

The basic working principle of the method, previously described in Ref. 63 and sketched in Fig. 11, includes the following key elements and functions: a sinusoidal signal at frequency f, on the order of a few tens of kHz, is fed to a loudspeaker oriented toward a directional microphone mounted in a fixed position at a distance d from the source. The phase difference $\Delta\phi$ between the source and the detected signals, measured by the computer, is proportional to the time delay between the signals, defined as $\Delta t = d/w$, i.e., by the ratio between the distance traveled by the sound wave and the speed of sound. However, if the distance remains unvaried, a single measurement of the phase does not provide sufficient information to determine the speed of sound. If instead the distance is made variable by placing the loudspeaker (or alternatively the microphone) on a moving stage whose position is controlled with a laser interferometer, the distance variation Δd may be determined with accuracy on the order of a few hundred nanometers. By contemporarily recording the interferometer reading of Δd and the consequent phase changes $\Delta\phi$ measured in radians, the speed of sound is obtained by the simple general relation:

$$w = \frac{2\pi f\,\Delta d}{\Delta\phi}. \tag{50}$$

Thus, given the selected frequency of the acoustic wave f, the speed of sound w may be directly obtained from a measurement of the

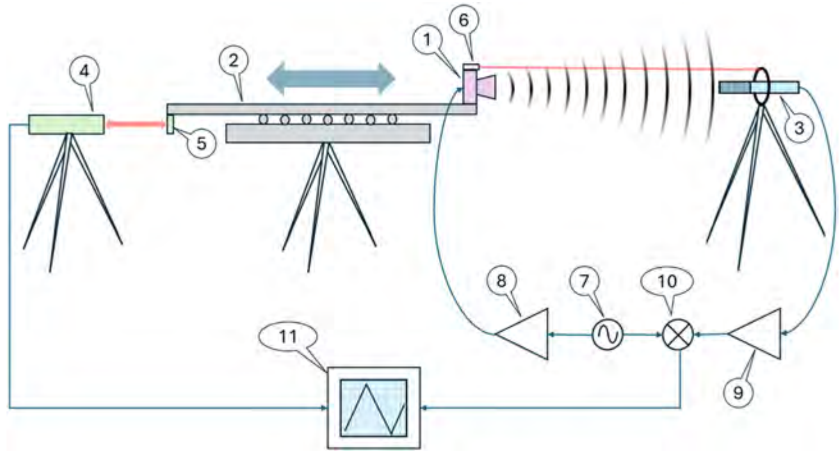

FIG. 11. Simplified sketch illustrating the working principle of the acoustic wavelength meter and its key components. A loudspeaker (1) mounted on a motorized carriage (2) emits a sound wave received by a microphone (3); a laser interferometer (4) pointing at a mirror (5) measures the movements of the carriage. An auxiliary laser (6) fixed to the loudspeaker serves to align the microphone to the measurement axis. A synthesizer (7) generates a sinusoidal signal that is sent to a power amplifier (8) that feeds the loudspeaker; the signal generated by the microphone is conditioned by the amplifier (9) and sent to a phasemeter (10) that compares the phase delay between the signals. The phase signal is recorded on a PC (11) together with the position measured by the interferometer.

slope of the dependence of the phase change over the distance, which is assumed to be linear. An alternative description of the method is by considering that a phase change $\Delta\phi = 2\pi$ occurs for every variation of the distance between the source and detector Δd that equals the wavelength λ of the sound wave, i.e., the instrument measures directly the sound wavelength by comparison with the wavelength of the laser interferometer used to measure the distance. That is in fact the working principle of a laser wavelength-meter[64] (or lambda-meter), justifying the name of *acoustic wavelength-meter* given to the setup used in this work.

3.1.2. Experimental setup

In this section, we provide a synthetic functional description with reference to Fig. 11, postponing a more detailed description to a separate publication.

The sound wave generator is a loudspeaker (dynamic tweeter loaded with an expansion horn, model Hertz ST 25A Neo) mounted on a motorized linear stage capable to travel 1 m stroke. The microphone is a supercardioid interference condenser model BOYA BY-PVM1000 with good directional performance, minimizing the sound coming from the sides and from the rear of the microphone. It is fixed on a tripod at a distance varying from 0.5 to 1.5 m from the loudspeaker, placed at the height of 130 cm from the floor. A synthesizer generates the ultrasound signal, at frequencies around 20 kHz, which is amplified and sent to the loudspeaker. Both the signal coming from the microphone and the signal generated by the synthesizer are sampled at 500 kHz and 16 bits prior to being sent to the computer. A laser interferometer is used to measure in real time the position of the linear stage with a resolution of 10 nm.

A LabView® software manages interface communication with the instrumentation, data analysis, and storage of the results.

The following auxiliary instruments complete the setup. A laser diode placed above the loudspeaker is aligned along the moving direction of the motorized carriage; it is used to place the microphone on the measurement axis. The abovementioned eight platinum thermometers are placed close to the measurement line equally spaced at the same height as the loudspeaker and the microphone. A 3-axes ultrasound anemometer is used to check the air flow induced by the conditioning system near the experiment. The experiment is run in an acoustic chamber set in semi-anechoic configuration, i.e., with a reflecting floor surface. To reduce possible interference of floor-reflected waves with the plane wave subject to measurement, a set of absorbing polyurethane foam prisms are placed on the floor in proximity to the experiment.

The carriage moves back and forth repeatedly for its 1 m long stroke at a constant speed of 12.5 mm/s; thus it takes 80 s to travel the whole stroke, which is considered as a single measurement run. The software measures the phase difference between the signal from the microphone and the signal sent to the loudspeaker. Hence, the phase changes $\Delta\phi$ are recorded together with the interferometer readings Δd during dozens of consecutive hours of acquisition. The software allows analysis of the collected data to calculate the slope of the phase versus distance curve for each measurement run. From the knowledge of the frequency f of the signal sent to the loudspeaker, we directly obtain the measurements of the speed of sound w.

An example of typical data acquisition is shown in Fig. 12. The black straight line represents the phase increment measured in degrees versus the distance covered by the carriage and measured by the interferometer in a single measurement run. The linear behavior of the phase increment is evident, and the fitting equation is reported on the figure. The slope value $\Delta\phi/\Delta d$ obtained by the fitting procedure allows the calculation of the speed of sound by using Eq. (50), after the measured phase increment is converted from degrees to radians. The typical estimation uncertainty of a single measurement run is 0.03 m s^{-1}, as detailed in Sec. 4.2. Hence, in the example of Fig. 12, w = (344.759 ± 0.043) m s^{-1}, considering the different uncertainty contributions from Sec. 4.2. In Fig. 12, the colored lines represent the residuals of ten sequential measurements from their respective linear fit.

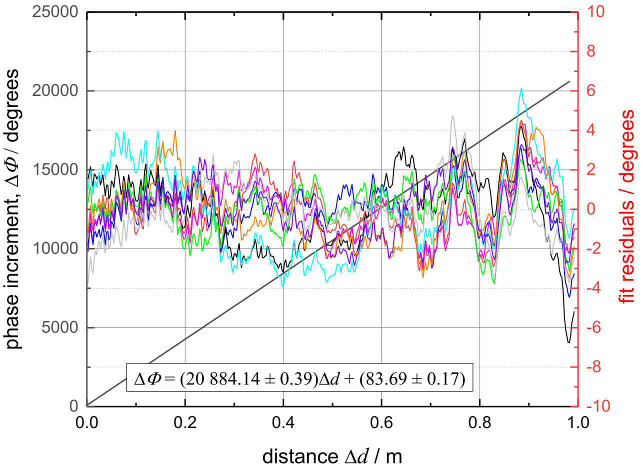

FIG. 12. Example of data acquisition and fit using the wavelength meter. The black straight line represents the measured phase changes versus distance (left scale); the colored lines are the residuals from the linear fit of 10 sequential measurements (right scale).

3.2. Acoustic resonator

The acoustic resonator used in this work is composed of two stainless steel (type 316LNR) hemispheres with nominally equal inner and outer radius of 81.5 and 96.5 mm. It had been previously used to achieve a determination of the Boltzmann constant k by measuring the speed of sound in helium at 273.16 K, and details about its construction and dimensional and shape characterization can be found in Ref. 65. Basically, it allows for both acoustic (ac) and microwave (mw) resonance measurements using two $1/4$ in. condenser microphones and two loop antennas. All these transducers are mounted flush with the internal surface of the cavity to minimize perturbations to the acoustic and electromagnetic field. Two gas inlet and outlet ducts, embedded in the antennas' supporting assemblies, allow flowing gas through the cavity, a possibility exploited in this work to continuously replace humid air from the acoustic test chamber by connecting to the gas inlet port a miniature membrane pump with a flow rate of ~4 l min^{-1}.

For both acoustic and microwave resonance frequency measurements, standard instrumentation and techniques were used, as described and discussed in Ref. 4. The relevant exceptions, which are of interest in this work, are discussed hereafter.

3.2.1. Microwave determination of internal radius

The resonator was assembled by fixing the position of the two comprising hemispheres to be slightly misaligned with respect to the vertical axis of the cavity. The resulting internal geometry differs from spherical, facilitating[66] the precise measurement of the average frequency of the triply degenerate microwave TM1n and TE1n modes, and can be approximated as a triaxial ellipsoid[67]

$$\frac{x^2}{\tilde{a}^2(1+\varepsilon_2)^2} + \frac{y^2}{\tilde{a}^2} + \frac{z^2}{\tilde{a}^2(1+\varepsilon_1)^2} = 1, \tag{51}$$

where $a = \tilde{a}[(1+\varepsilon_1)\,(1+\varepsilon_2)]^{1/3}$ is the reference mean internal radius of the cavity, and the *deformation* parameters ε_1 and ε_2 measure the relative difference of the ellipsoid semi-axes.

To determine the cavity radius $a(T)$ at some reference temperature T_{ref}, the resonator was initially inserted in a large volume (30 cm i.d., 50 cm length) stainless steel vessel set to vertically stand on the floor of the test chamber. The average resonance frequencies $\langle f_{\mathrm{mw}}(0,T)\rangle$ of eight microwave modes (TM11 to TM14, TE11 to TE14) were fitted and recorded for about 150 hours with the vessel and the cavity under vacuum while the temperature of the cavity drifted between 292.5 K and 294.5 K. The last ten hours of this record happened to be more thermally stable, and were considered for further analysis, first by correcting the recorded resonance frequencies to exactly $T_{\mathrm{ref}} = 294.00$ K

$$\langle f_{\mathrm{mw}}(0, T_{\mathrm{ref}})\rangle = \langle f_{\mathrm{mw}}(0, T)\rangle[1 + \alpha_{\mathrm{th}}(T - T_{\mathrm{ref}})], \tag{52}$$

where the thermal expansion coefficient of 316-LNR type stainless steel $\alpha_{\mathrm{th}} = (16.9 \pm 0.5) \times 10^{-6}\ \mathrm{K}^{-1}$ is inferred from the full measurement record. The internal radius of the cavity in vacuum $a(0, T_{\mathrm{ref}})$ is determined as

$$a(0, T_{\mathrm{ref}}) = \frac{c_0 z_{\mathrm{mw}}}{2\pi\langle f_{\mathrm{mw}}(0, T_{\mathrm{ref}})\rangle}, \tag{53}$$

where $c_0 = 299\,792\,458\ \mathrm{m\ s}^{-1}$ is the exact definition of the speed of light in vacuum[68] and the eigenvalues z_{mw} differ from those of a perfect sphere and are corrected by the model[69] to account for the shape of the cavity defined by Eq. (51), with $\varepsilon_1 = (1.49 \pm 0.02) \times 10^{-3}$ and $\varepsilon_2 = (0.84 \pm 0.01) \times 10^{-3}$ being experimentally estimated by measuring the relative separation of the three components of the mw resonances. These relative corrections range between a minimum of 0.3 ppm for mode TM11 and a maximum of 9.8 ppm for mode TE14 with negligible uncertainty contribution to the determination of $a(0, T_{\mathrm{ref}})$.

Corrections for the finite penetration of the electromagnetic field into the cavity wall, relatively ranging between 99 ppm for mode TM11 and 32 ppm for mode TE14, are calculated based on the maximum electrical conductivity $\sigma_{\mathrm{exp}} = 1.146\ \mathrm{S\ m}^{-1}$ estimated from the mode halfwidths. Alternatively, the reference value $\sigma_{316} = 1.228\ \mathrm{S\ m}^{-1}$ determined in Ref. 70 can be used. Choice between these alternatives makes a small relative contribution of 1.2 ppm to the uncertainty of the determination of $a(0, T_{\mathrm{ref}})$.

An additional correction to the mw frequencies was applied to account for two 4 mm diameter epoxy-filled holes surrounding antennas within the supporting steel mounts. The correction, relatively on the order of 2.5 ppm, was calculated based on the perturbation model illustrated in Ref. 71. Before the acoustic measurements in air discussed below, the antenna mounts were replaced by the models described in Ref. 70 with the hole surrounding the antenna reduced to 0.8 mm. An additional uncertainty contribution of 5 ppm conservatively accounts for the possible change in the internal volume of the cavity resulting from this replacement.

TABLE 6. Uncertainty budget for the microwave determination of the resonator radius in vacuum at 294 K

Uncertainty source	St. unc. of $a(0, 294\ \mathrm{K})$ mm	Rel. st. unc. of $a(0, 294\ \mathrm{K})$ ppm
Discrepancy among different microwave modes	0.000 60	7.4
Imperfect positioning of antenna mounts	0.000 41	5.0
Vertical thermal gradient across the cavity	0.000 27	3.4
Alternative estimates of electrical resistivity	0.000 11	1.2
Quadrature sum	**0.000 79**	**9.6**

After these corrections, the final estimate of the mean internal radius of the cavity in vacuum at 294 K, $a(0, 294\ \mathrm{K}) = (81.465\,95 \pm 0.000\,79)$ mm, is obtained as the weighted mean of the results from eight mw modes, with weights proportional to the combined contribution of fitting precision, standard deviation of repeated measurements, and excess halfwidth of each mode. The standard uncertainty reported for $a(0, 294\ \mathrm{K})$ is the quadrature sum of the relative contributions listed in Table 6.

The standard deviation of more than 100 repeated records of the mw resonance frequencies, temperature-corrected with Eq. (52), ranges from a minimum of 2.5 parts in 10^8 for mode TE12 to a maximum of 3.6 parts in 10^7 for mode TE14, making a negligible uncertainty contribution to the determination of $a(0, 294\ \mathrm{K})$.

The results obtained from mode TM11 were found to differ systematically by 15 ppm from the average of the other modes, themselves all relatively dispersed by less than 2.5 ppm (see Fig. 13). TM11 mode is also characterized by a larger relative excess halfwidth (2.5 ppm compared to a maximum of 0.7 ppm for all the other modes), contributing less than 1/10 to the weighted mean of $a(0, 294\ \mathrm{K})$. Conservatively, we assume half of the relative discrepancy of mode TM11 as the most relevant contribution to the uncertainty budget.

A rather large vertical thermal gradient was observed during mw measurements of the cavity volume in vacuum, with the bottom part of the resonator warmer by 0.2 K than the top. In proportion to the thermal expansion coefficient $\alpha_{\mathrm{th}} = 16.9 \times 10^{-6}\ \mathrm{K}^{-1}$, the imperfect estimate of the temperature of the cavity makes an additional relative uncertainty contribution of 3.4 ppm to the determination of $a(0, 294\ \mathrm{K})$.

Relative to its vacuum reference value, the internal radius decreases linearly as a function of pressure when the cavity and the surrounding volume are exposed to gas, requiring a correction proportional to the isothermal compressibility of steel $\kappa_T = (3/a)(\mathrm{d}a/\mathrm{d}p)$. A previous experimental estimate[65] $\kappa_T = 6.3 \times 10^{-12}\ \mathrm{Pa}^{-1}$ is used here, leading to a relative correction of about

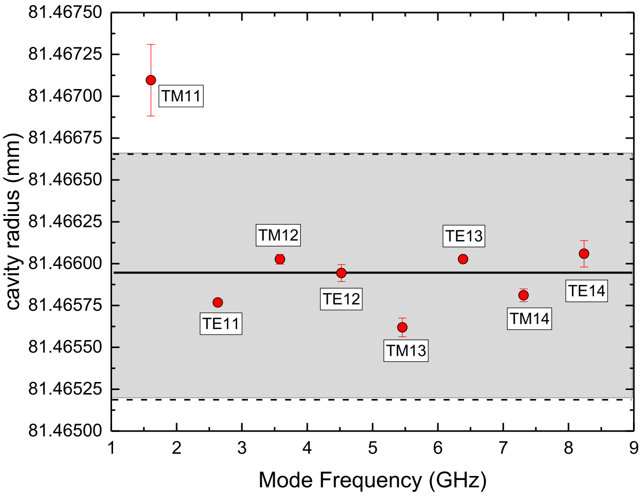

FIG. 13. Internal resonator radius in vacuum at 294 K determined from measurements with eight microwave modes. The uncertainty bars display the combined contribution of mean resonance fitting precision, standard deviation of repeated measurements, and residual excess halfwidths after skin correction. The black line and gray-shaded area display weighted mean radius and standard uncertainty with contributions listed in Table 6.

0.2 ppm at ambient pressure. Finally, our reference function for the cavity radius $a(p, T)$ as a function of temperature and pressure is

$$a(p,T) = a(0,294\,\mathrm{K})[1+\alpha_{\mathrm{th}}(T-294\,\mathrm{K})]\left(1+\frac{\kappa_T}{3}p\right)^{-1}. \tag{54}$$

3.2.2. Acoustic measurements and model of the resonator

At each thermodynamic state realized in the test chamber, defined by the measured variables pressure, temperature, relative humidity, and CO_2 concentration (p, T, h_r, x_{CO2}), the speed of sound w was determined at several different frequencies $f_{\mathrm{ac}} = f_{(0,\,n)}$ corresponding to the resonance frequencies of up to eight purely radial acoustic modes, namely (0,2) to (0,8) and (0,10), spanning the overall frequency range between 3 kHz and 20 kHz, while mode (0,9) was found too overlapped by neighboring modes in the acoustic spectrum to be precisely measurable. Approximate values of the acoustic resonance frequencies $f_{(0,\,n)}$ and half-widths $g_{(0,\,n)}$ were obtained from preliminary measurements. Then, the source microphone driven by a frequency synthesizer was stepped around the resonance curve of each mode at 11 discrete frequencies, covering the interval $f_{(0,\,n)} \pm 2g_{(0,\,n)}$, and the in-phase and quadrature signals at the detector microphone are measured using a lock-in amplifier The set of frequencies and complex voltages are fitted by a suitable resonance function with 10 adjustable parameters [see Eq. (7) in Ref. 4] to provide an estimate of f_{exp} and g_{exp}. The typical relative fitting precision varied between a minimum of 0.2 ppm for narrow, well-isolated, low-order radial modes like (0,4) to nearly 4 ppm for mode (0,10) which is significantly enlarged by absorption. The acquisition of a complete dataset for eight radial modes required ~6 min.

Based on the reference internal cavity radius $a(p, T)$ discussed above, experimental determinations of speed of sound in air w_{exp} are calculated as

$$w_{\mathrm{exp}}(p,T,h_r,x_{CO2}) = 2\pi a(p,T)\, f_{\mathrm{ac}}(p,T,h_r,x_{CO2})/z_{\mathrm{ac}}, \tag{55}$$

where the acoustic eigenvalues z_{ac} are determined, using perturbation theory,[72] by the deformation parameters ε_1 and ε_2, resulting in relative differences from the eigenvalues of a perfect sphere up to 35 ppm for mode (0,10). In Eq. (55), the unperturbed frequencies f_{ac} ideally refer to a cavity with infinite acoustic impedance filled with a non-dissipative gas. Thus, they must be derived from f_{exp}, i.e., the frequencies determined experimentally by fitting resonance curves, as $f_{\mathrm{ac}} = f_{\mathrm{exp}} + \Delta f$ upon applying corrections Δf to account for relevant perturbations. Among these, the thermal boundary layer near the cavity surface plays a major role, with relative corrections Δf_{th} of ~100 ppm for mode (0,2) and 40 ppm for mode (0,10) at ambient temperature and pressure. In principle, the thermal conductivity of humid air $\kappa_{\mathrm{th}}^{\mathrm{wet}}$ is needed for accurate calculation of the corrections, though correlations and experimental estimates of this quantity are scarcely available. However, for the conditions of temperature, pressure, and humidity of the test chamber, with the molar fraction of water vapor not exceeding $x_w = 0.015$, the relative difference between $\kappa_{\mathrm{th}}^{\mathrm{wet}}$ and $\kappa_{\mathrm{th}}^{\mathrm{dry}}$, the thermal conductivity of dry air at the same temperature, is estimated to be well within 2%.[73,74] Thus we may assume the reference equation[75] for $\kappa_{\mathrm{th}}^{\mathrm{dry}}$ as an adequate replacement for $\kappa_{\mathrm{th}}^{\mathrm{wet}}$ with negligible additional uncertainty to the calculation of thermal boundary corrections. A secondary thermal boundary layer perturbation to f_{ac} occurs due to imperfect thermal accommodation at the gas–solid interface. This relative perturbation does not depend on frequency and increases in proportion to p^{-1}. Since a reliable estimate of the thermal accommodation coefficient h for humid air is not available from theory or dedicated experiments, here we simply assume $h = 1$ for air, with a resulting correction to f_{exp} of 0.7 ppm. The assumption is supported by results[76] which set $h = 0.85$ as an average value of h for nitrogen in contact with different metal surfaces. We remark that the rather different choice $h = 0.3$ would change the relative correction to f_{exp} by only 3.5 ppm, with a negligible uncertainty contribution to our determination of the speed of sound.

In addition to boundary effects, our perturbation model accounts for coupling between the acoustic pressure of the gas within the cavity and elastic vibrations in the shell. We calculated the corresponding shell corrections to f_{exp} using the model of Mehl[77] and tabulated values of the elastic properties of 316 stainless steel[78] to predict the lowest radial resonance in the shell $f_{\mathrm{br}} \sim 15.0$ kHz, which falls about midway between the radial modes (0,7) and (0,8) in the acoustic spectrum. An alternative finite-element method (FEM) model[65] predicts $f_{\mathrm{br}} \sim 14.2$ kHz which is closer to mode (0,7) than (0,8), but we did not find experimental evidence of a larger perturbation for mode (0,7). Thus, we applied corrections to f_{exp} based on Refs. 77 and 78, which span between a relative minimum of −1.7 ppm for mode (0,2) and 12.8 ppm for mode (0,8), and include the difference from the corrections resulting from the alternative model[65] as an additional uncertainty contribution to our speed of sound determination.

Corrections to account for other minor perturbations, such as those due to the finite impedance of the microphone surface and the ducts surrounding the antennas, were not implemented, though their approximate estimate, based on previous modeling of these effects for the same cavity when filled with He,[65] sets an upper limit, on the order of 5 ppm, to the uncertainty contribution of this simplification

Energy losses take place in the boundary layer near the internal cavity surface and in the bulk of the gas, both contributing to the acoustic resonance halfwidths. Bulk effects prevail at higher frequencies, caused by different absorption mechanisms, namely *classical* thermo-viscous dissipation, rotational relaxation, and vibrational relaxation. Their combined effect defines an absorption (or attenuation) coefficient $\alpha = \alpha_{\mathrm{cl}} + \alpha_{\mathrm{rot}} + \alpha_{\mathrm{vib}}$, which is readily calculable as a function of p, T, h_{r}, and f using the standard equations worked out to quantify sound absorption in the atmosphere:[38]

$$\alpha_{\mathrm{cl}} + \alpha_{\mathrm{rot}} = 1.84 \times 10^{-11} f^2 \frac{p_{\mathrm{r}}}{p} \left(\frac{T}{T_{\mathrm{r}}}\right)^{0.5}, \tag{56}$$

$$\begin{aligned}\alpha_{\mathrm{vib}} = f^2 \left(\frac{T}{T_{\mathrm{r}}}\right)^{-5/2} \Bigg[& 0.012\,75 \exp\left(\frac{-2239.1}{T}\right)\left(\frac{f_{\mathrm{O2}}}{f_{\mathrm{O2}}{}^2 + f^2}\right) \\ & + 0.010\,68 \exp\left(\frac{-3352.0}{T}\right)\left(\frac{f_{\mathrm{N2}}}{f_{\mathrm{N2}}{}^2 + f^2}\right)\Bigg].\end{aligned} \tag{57}$$

In Eqs. (56) and (57), which define the absorption coefficient α in m^{-1}, $p_{\mathrm{r}} = 101.325$ kPa, $T_{\mathrm{r}} = 293.145$ K, and f_{O2} and f_{N2} are the relaxation frequencies of molecular oxygen and nitrogen respectively, previously defined in Sec. 2.2.4, with uncertainties discussed in Sec. 2.3.

Altogether, the above assumptions define our model for the analysis of acoustic data measured by the resonator.

4. Comparison of Experimental Determinations of Speed of Sound in Air with Theory

4.1. Acoustic wavelength meter results and comparison with theory

In order to compare the experimental measurements of the speed of sound with the theoretical model, it is necessary to measure the environmental parameters in the chamber synchronously with the speed of sound measurements. The readings of the 8 platinum thermometers are recorded every 20 s, while the other environmental parameters, which vary more slowly, such as the atmospheric air pressure, the carbon dioxide mole fraction, and the relative humidity of air, are recorded every 6 min. Then, all the recorded environmental parameters are resampled, using a dedicated software algorithm developed in LabVIEW®, to adjust their synchronicity with the measurement of the speed of sound.

The results of typical measurement sessions, showing the experimental records for several hours of consecutive speed of sound measurements taken every 80 s, are shown in Fig. 14, where the comparison with the corresponding prediction from the model discussed in Sec. 2 is also illustrated by plotting the relative difference between experiment and theory. Particularly, the left plot in Fig. 14 shows a case where the temperature in the anechoic chamber is naturally slowly drifting, before the conditioning system is switched on and the temperature decreases suddenly from 292.5 to 286 K in about 80 min. At the same time, the other recorded environmental parameters were $39\% < h_{\mathrm{r}} < 53\%$ and $462\ \mathrm{ppm} < x_{\mathrm{CO2}} < 486\ \mathrm{ppm}$, while the atmospheric pressure was approximately constant at 99.0 kPa. The acoustic frequency was 20 kHz. As a consequence of switching on the conditioning system, an increase of the fluctuations and noise affecting the measured speed of sound is clearly visible. In spite

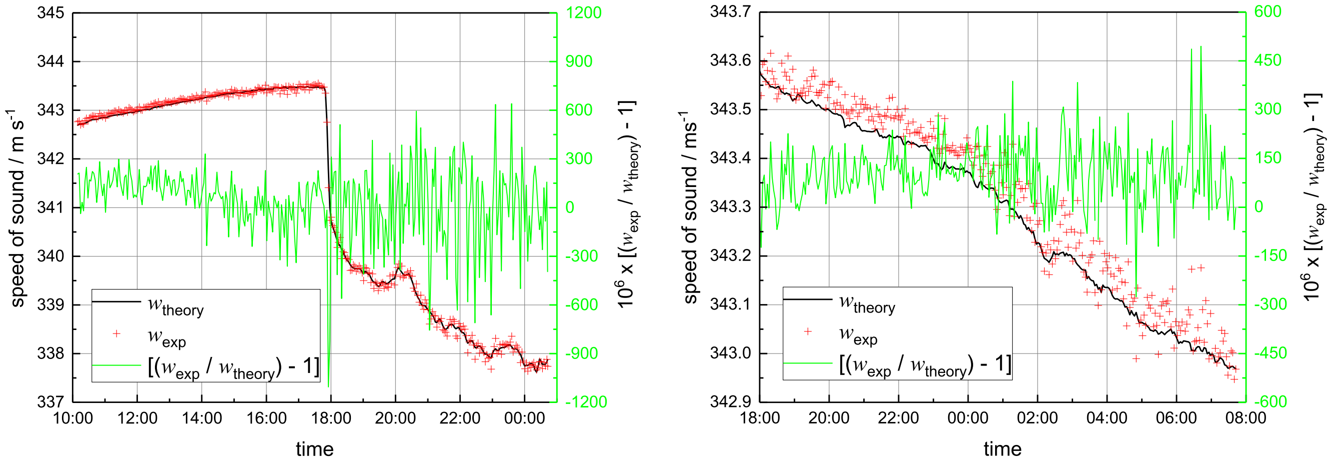

FIG. 14. Examples of speed of sound results obtained by the λ-meter during typical measurement sessions. The speed of sound w_{exp}, recorded every 80 s (red cross symbols), is compared to the speed of sound w_{theory} calculated using the model developed in this work (black line). The relative difference between experiment and theory is plotted in green (right scale). (Left panel) The temperature regulating system of the test chamber is turned on just before 18:00 time reference. Before this reference, air temperature in the chamber is increasing slowly, immediately after it decreases abruptly. (Right panel) The temperature of the chamber decreases by 0.8 K during 14 h, while other environmental parameters undergo minor variations. Relative differences between experiment and theory are on the order of 100 ppm, with a standard deviation of 95 ppm.

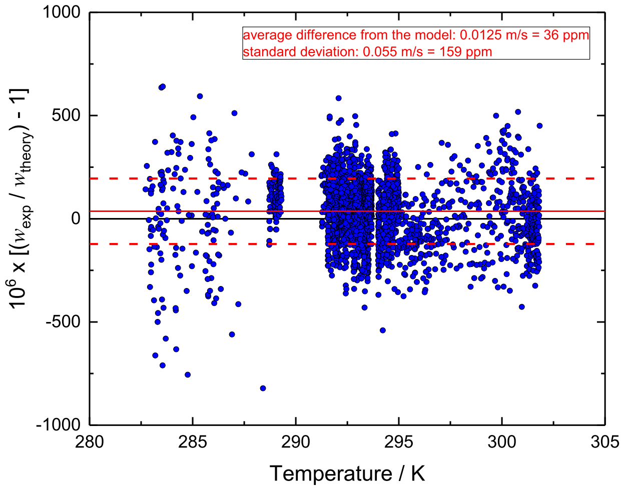

FIG. 15. Relative deviations between experimental determinations of the speed of sound in air obtained using the λ-meter and predicted values from the model presented in this work. The red solid and dashed lines respectively represent the mean relative difference (36 ppm) and the standard deviation (159 ppm) of the whole measurement set, spanning a temperature range between 284 K and 301 K.

of this abrupt change, the agreement between experimental determinations w_{exp} and model predictions w_{theory} is satisfactory, with the model-calculated speed of sound faithfully tracking experimental determinations and relative differences $(w_{\text{exp}} - w_{\text{theory}})/w_{\text{exp}}$ well within 300 ppm.

The right plot in Fig. 14 shows a measurement run where the temperature of the chamber remains nearly constant as a function of time, but for a smooth slow regular temperature decrease from 292.4 to 291.6 K during 14 h, resulting in a temperature gradient of ~1 mK/min. Over the same time lapse, the variation of other recorded environmental parameters was 99.6 kPa < p < 99.7 kPa, 43% < h_r < 50%, and 482 ppm < x_{CO2} < 557 ppm. Again, the agreement between experiment and model is satisfactory with relative differences on the order of 100 ppm and a standard deviation of 95 ppm.

Figure 15 displays a complete collection of all the experimental speed of sound measurements obtained using the λ-meter over a period of time lasting several weeks, while the temperature in the chamber varied over a range of nearly 20 K, approximately spanning 284–301 K. Over the same period of time, the total span of relative humidity and CO_2 fraction was 30% < h_r < 60%, 400 ppm < x_{CO2} < 700 ppm. The lower temperature conditions in the chamber could be realized by inlet of cool air from outdoors in concurrent winter season, while the highest end of the temperature range was achieved by setting different heating powers through the chamber conditioning system. Each point in Fig. 15 plots the relative difference $(w_{\text{exp}} - w_{\text{theory}})/w_{\text{exp}}$ between a single speed of sound measurement using the λ-meter and the theoretical estimate of the model presented in this work. As already observed in Fig. 14, it can be noted that the dispersion of the measurement results is larger for lower temperatures, when the conditioning system is on. Otherwise, the overall quality of the agreement between experiment and theory is indeed remarkable with a mean difference of 0.012 m s^{-1} and a standard deviation of 0.055 m s^{-1}.

4.2. Acoustic wavelength meter uncertainty budget

The wavelength meter experiment realized in this work is one of a kind, with no previous published examples to guide the evaluation of the uncertainty budget. Therefore, we did our best to consider all possible sources of uncertainty, by performing several specific experimental tests and evaluation to assess their possible influence. The detailed description of each of these tests and evaluations is too long to be included in the present work and will be the object of a separate publication.

Table 7 lists the complete uncertainty budget, with separate entries for the absolute and relative standard uncertainty of each contribution. There, we make a distinction between contributions affecting the experimental method and those related to our imperfect estimate of the environmental parameters (temperature, humidity, CO_2 concentration) in the test chamber. One reason for this distinction is to facilitate the comparison of two experimental methods, the λ-meter and the acoustic resonator, as discussed in Sec. 4.4, because these methods have different experimental errors but are otherwise fully correlated by the imperfect estimate of the environmental conditions. These errors should therefore not be considered for the mutual comparison of the two experiments, but should be included when the results obtained with each experiment are compared to the predictions of the theoretical model.

A brief description and discussion on the methods and input data supporting the estimate of the uncertainty contributions in Table 7 is provided in the remainder of this section.

Measurement precision is mainly affected by air turbulence and is estimated to vary between 0.024 m s^{-1} and 0.035 m s^{-1}, by the standard deviation of consecutive repeated measurements at steady temperature conditions. Taking the largest value as a reference, we consider that a single measurement result can practically be obtained by averaging 100 consecutive runs, under the assumption that they would be normally distributed, thus reducing by a factor of 10 the standard deviation of the mean to 0.0035 m s^{-1}, or relatively 10.2 ppm.

Interferometer reading: this contribution comes from the uncertainty associated with the determination of the laser wavelength, requiring an estimate of the refractive index of air that depends on temperature. Conservatively, we assume the uncertainty of our estimate of air temperature to be on the order of 0.1 K, with a resulting relative contribution, according to Edlén,[79] to the uncertainty in the determination of the displacement of about 0.1 ppm.[80]

Alignment errors: this is the largest contribution to the experimental uncertainty and includes the possible error associated with the estimation of the real distance change between the microphone and the loudspeaker, induced by possible misalignments between the acoustic measurement axis and the interferometer measurement axis. The ideal measurement axis is assumed to be the virtual straight line passing through the center of the loudspeaker and running parallel to the axis of the carriage. An auxiliary laser fixed to the loudspeaker is used to materialize this line (see Fig. 11). In order to investigate the contribution of alignment errors, the measurements were repeated by changing the position of the microphone

TABLE 7. Uncertainty budget of the wavelength meter

Uncertainty contribution	Value and unit	$u(w_{\mathrm{exp}})$ standard uncertainty contribution (m s^{-1})	$u_{\mathrm{r}}(w_{\mathrm{exp}})$ relative standard uncertainty contribution (ppm)
Measurement precision[a]	0.035 m s^{-1}	0.003 5	10
Optical interferometer wavelength	0.10 μm	0.000 034	0.1
Optical interferometer geometrical errors	see text	0.027	79
Acoustic interference	0.005 m s^{-1}	0.005	15
Acoustic frequency	0.04 Hz	0.000 7	2
Regression error of phase/distance slope	0.29 deg m^{-1}	0.004 8	14
Air flow speed	0.0144 m s^{-1}	0.014 4	42
Exp. method uncertainty		**0.031**	**92**
Thermometry calibration	0.005 K	0.003	8.7
Temperature fluctuation	0.010 K	0.006	18
Temperature gradients	0.02 K	0.012	34
Relative humidity	2%	0.027	80
CO_2 concentration	80 ppm	0.009	25
Environmental uncertainty		**0.032**	**92**
Total quadrature sum		**0.045**	**130**

[a] The reported contribution is for a single measurement run; the reported standard uncertainty is based on averaging 100 consecutive measurements.

with respect to the ideal measurement axis. The results obtained in the misaligned configuration allow us to estimate the relative uncertainty contribution due to possible alignment errors to be on the order of 80 ppm.

Acoustic interference: reflection of acoustic waves from the chamber floor may interfere with the detected wave front. In order to reduce this effect, a supercardioid microphone was chosen because of its directionality and better isolation from room noise. Nevertheless, we investigated the effect of spurious reflections by placing a number of foam prisms on the floor along the acoustic path. We varied the number and the position of the absorption prisms in different random arrangements, and we evaluate the uncertainty contribution due to the possible acoustic interference as the dispersion of the speed of sound values measured in the different configurations.

Acoustic frequency: the reported estimate is based on the maximum error specification of the synthesizer.

Regression error: the slope of the fitting curve, while assumed nominally linear, is in practice affected by nonlinearity and noise. The example plotted in Fig. 12 shows that typical residuals from the linear fit are on the order of a few degrees, with the standard uncertainty of the fit on the order of 0.29 deg/m leading to an uncertainty of about 14 ppm.

Speed of air flow: the movement of air in the direction of the acoustic path directly adds to the speed of sound and thus represents an important contribution, especially in the case of outdoor measurements. Actually, the effect is even more complicated to evaluate, since air could flow in any direction with respect to the acoustic path, causing a shift of the sound wavefront that affects the detected signal. An example of the analysis of the influence of air movement on sound propagation is reported in Ref. 80. For our measurement conditions, the effect of air movement has been evaluated by using a three-dimensional ultrasonic anemometer (WindMaster, manufactured by Gill Instruments) to experimentally measure the direction and the intensity of air flow. From averaged readings of air speed, assuming the associated distribution as rectangular, we estimate the equivalent standard deviation at 0.015 m s^{-1}.

Thermometer calibration: the listed contribution corresponds to the standard calibration uncertainty of the IPRTs deployed along the acoustic path of the λ-meter.

Temperature fluctuations: here we consider the maximum difference between the readings of several thermometers along the acoustic path, presumably induced by air flow fluctuations.

Vertical and horizontal temperature gradients: thermometers are not placed along the sound path, so as not to disturb the traveling wave, but positioned several centimeters apart; thus, the temperature of the volume of air between the loudspeaker and the microphone can be slightly different and this mainly depends on the temperature gradients in the chamber. The horizontal temperature gradient was measured by means of the 6 IPRTs deployed orthogonally to the acoustic path every 20 cm, while the vertical temperature gradient was measured by using the same thermometers deployed vertically starting from 50 cm from the floor

Relative humidity and CO_2 concentration uncertainty contributions are based on the specification of the measuring instrument discussed in Sec. 3.

4.3. Acoustic resonator results in comparison with theory

The validity of the acoustic model of the resonator, previously discussed in Sec. 3.2.2, and its overall performance for speed of sound measurements in humid air, can be tested by comparison of the determination w_{exp} obtained with this instrument with the theoretical prediction w_{theory} of the same quantity using the thermodynamic model discussed in Sec. 2 in a mutual validation process. To exemplify the typical measurement conditions and a preliminary assessment of such comparison, we consider two measurement runs. The first run refers to stable thermodynamic conditions in the test chamber, with $T \sim 294.73$ K, before the chamber temperature regulation system is turned on, resulting in a rapid temperature increase. In the left plot of Fig. 16, the theoretical prediction of the speed of sound is plotted as a function of time for two different frequencies, at 3.03 and 20.1 kHz respectively. These frequencies bound the frequency range of variation of f_{ac} of seven radial modes (0,2) to (0,6), (0,8), and (0,10), used for the determination of w_{exp}. The plotted comparison with theory shows remarkable agreement of the model with the experiment, and comparable dispersive intervals as a function of frequency.

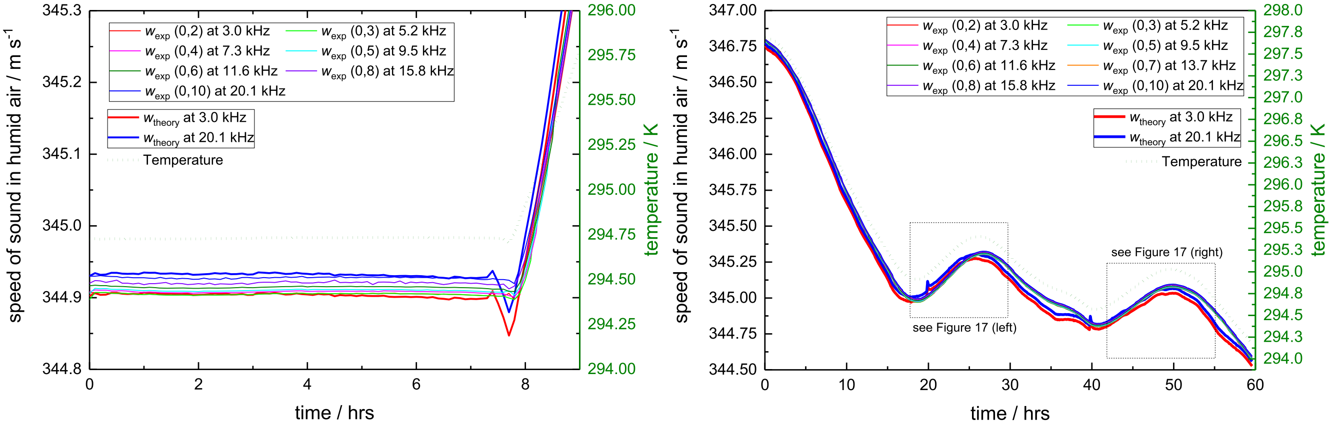

FIG. 16. Comparison of measured sound speeds with model. Left panel: comparison of theoretically calculated w_{theory} and experimentally measured w_{exp} speed of sound in humid air with initially stable conditions in the test chamber before start of the temperature regulation system. Right panel: comparison of w_{theory} and w_{exp} measured, over a time lapse of 60 h, with the test chamber temperature regulation system on. Magnified details of the measurement run are shown in Fig. 17.

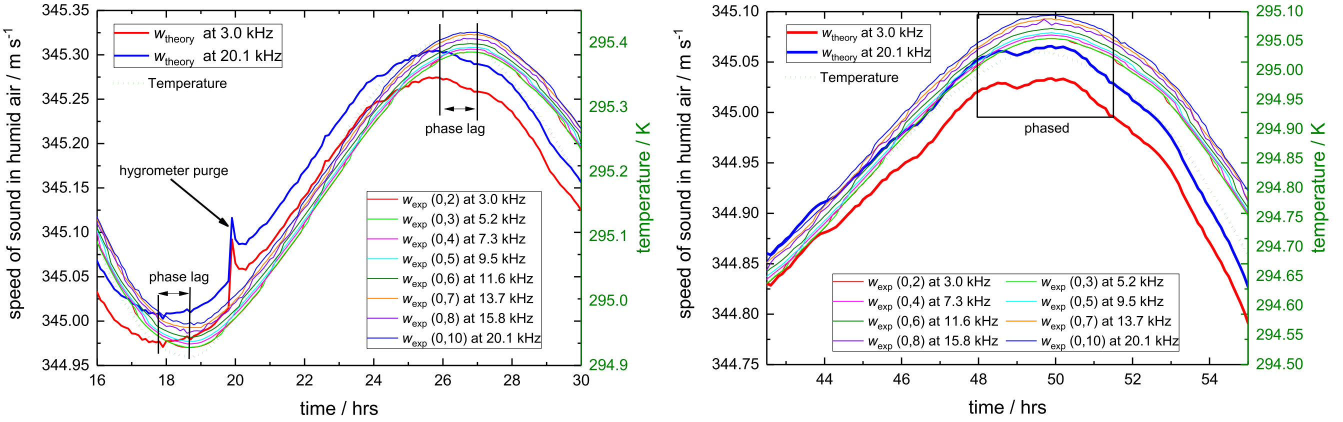

FIG. 17. Comparison of calculated w_{theory} and experimental w_{exp} speed of sound in humid air for selected intervals within the complete dataset in Fig. 16. (Left plot) The acoustic response w_{exp} of the resonator lags behind the temperature change recorded by thermometers on the cavity wall and used to calculate w_{theory}. Estimates of relative humidity in the test chamber are disturbed by automated purging operation of the hygrometer, which affect the calculation of w_{theory} but are not evident on the traces of w_{exp}. (Right plot) Example of data selected for comparison of w_{theory} and w_{exp}, in conditions of good temperature stability and well-phased agreement between thermometer readings and acoustic temperature.

The second example measurement run, shown in the right plot of Fig. 16, was recorded over 60 h, while the temperature of the test chamber decreased on average, but with subsequent diurnal oscillations, between ~298 K and 294 K. Over the same period, the variation of other recorded environmental parameters was 99.4 kPa $< p <$ 100.2 kPa, 39% $< h_r <$ 43%, and 510 ppm $< x_{CO2} <$ 570 ppm. As a whole, the record shows a good qualitative agreement of the model with experimental data from eight radial modes, with close-tracking overlapping trends, and comparable dispersive intervals as a function of frequency. A precise quantitative assessment of the agreement is more difficult due to the variable time lag by which the resonator, due to its rather large heat capacity, follows the changing environmental conditions in the test chamber, as shown by the magnified portions of the same plot in Fig. 17.

To enhance the meaningfulness of the comparisons between w_{exp} and w_{theory}, we considered subsets from the full dataset recorded in the text chamber, with the requirement that temperature be sufficiently stable, as normally happens close to the maxima and minima of temperature variation and, additionally, by checking that the trend of speed of sound measurements with the resonator would be sufficiently in phase with that of the temperature recorded from thermometers embedded in the cavity wall. Two such instances correspond to the data shown in the left plot of Fig. 16 and the right plot of Fig. 17.

For these selected measurements, we first consider the adequateness and completeness of our model of the acoustic field in the resonator by comparison of g_{exp} and g_{calc}, respectively the experimental and theoretical halfwidths of the resonances used to measure speed of sound at different frequencies in the range 3–20 kHz. As discussed above, the resonance halfwidths $g_{\text{calc}} = g_{\text{th}} + g_{\text{abs}}$ have two major contributions, namely $g_{\text{th}} = \Delta f_{\text{th}}$ from the loss of heat in the thermal boundary layer and, from bulk absorption, $g_{\text{abs}} = w\alpha/2\pi$, where the absorption coefficient α is defined by Eqs. (56) and (57).

At the measurement conditions considered here, g_{th} spans between 0.32 Hz for mode (0,2) and 0.82 Hz for mode (0,10), while g_{abs} spans between 0.13 Hz for mode (0,2) and 3.54 Hz for mode (0,10). Figure 18 plots the relative excess halfwidths $(g_{\text{exp}} - g_{\text{calc}})/f$ of seven to eight purely radial modes of the resonator, found to vary between a minimum of 8.6 ppm for mode (0,6) and a maximum of 33 ppm for mode (0,10). These characteristic figures measure the adequateness of our acoustic model and provide a plausible estimate of a main uncertainty contribution to our experimental determination of the speed of sound.

For the same selected data, Fig. 19 shows a comparison between the predicted speed of sound in air w_{theory} and the experimentally determined w_{exp}, as a function of frequency. The standard uncertainty of the model w_{theory} varies between 22 ppm at 3 kHz and 26 ppm at 20 kHz.

4.4. Acoustic resonator uncertainty budget

For the stable measurement run shown in the left panel of Fig. 16, the uncertainty budget of w_{exp} is detailed in Table 8. There, we distinguish between uncertainty contributions that are inherent to the experimental method itself and those arising from the imperfect estimate of the thermodynamic conditions in the test chamber and the cavity. The former category includes the uncertainty of the microwave determination of the radius, the imperfect estimate of shell coupling perturbations, and the overall adequateness of the acoustic model estimated by the excess halfwidths displayed in Fig. 18. The latter category has the two mostly relevant contributions, relatively about 80 ppm and 60 ppm respectively, from the imperfect estimate of relative humidity in the chamber and the thermal gradient measured by two thermometers mounted on the resonator. Remarkably, the model estimates of w_{theory} and the measured w_{exp} are found consistent within their combined standard uncertainty over the whole

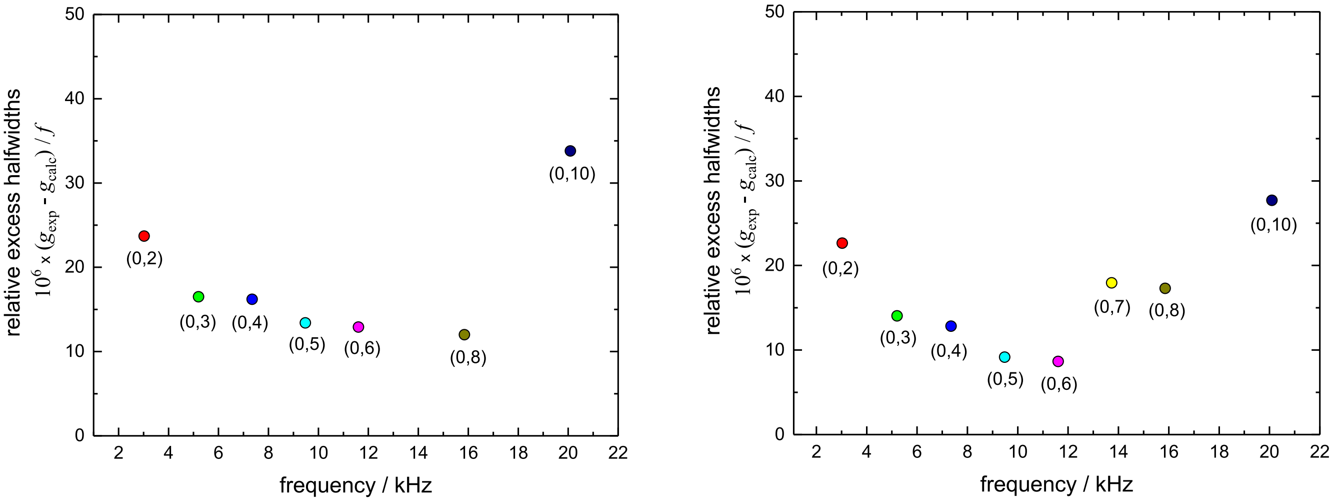

FIG. 18. Relative excess halfwidths $(g_{\text{exp}} - g_{\text{calc}})/f$ of seven to eight radial modes used to measure speed of sound in humid air. Left plot: data extracted from measurement run displaying in left panel of Fig. 16, with T = 294.73 K, p = 99.55 kPa, h_r = 44.1%, and x_{CO2} = 464 ppm. Right plot: data extracted from measurement run displaying in Fig. 17 (right panel), with T = 295.02 K, p = 99.61 kPa, h_r = 41.4%, and x_{CO2} = 550 ppm.

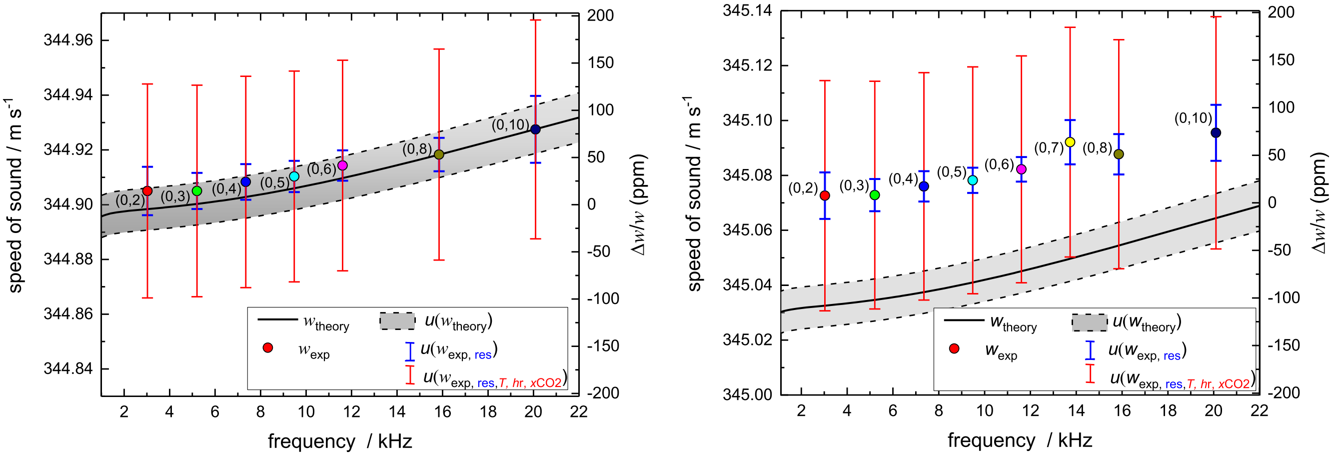

FIG. 19. Comparison of calculated w_{theory} and experimental w_{exp} measurements of speed of sound in humid air for the same data and measurement runs displayed in Fig. 16 (Left panel) and Fig. 17 (Right panel). For theory, the black line and the gray shaded area respectively display w_{theory} and its standard uncertainty. For the experiment, the inner (blue) uncertainty bar is the quadrature sum of the main contributions related to the determination of w_{exp} with the resonator method. The outer (red) uncertainty bars display the overall uncertainty, which additionally includes contributions from the imperfect estimate of the thermodynamic conditions (temperature, humidity, CO_2 concentration) in the cavity and the test chamber.

TABLE 8. Uncertainty budget for the acoustic determination of the speed of sound in humid air w_{exp} shown in the left panel of Fig. 16. T = 294.73 K, p = 99.55 kPa, h_r = 44.1%, and x_{CO2} = 464 ppm for seven radial modes with frequencies between 3.0 kHz and 20.1 kHz.

Uncertainty source	Relative uncertainty contribution to w_{exp} (ppm)						
Mode order	(0,2)	(0,3)	(0,4)	(0,5)	(0,6)	(0,8)	(0,10)
Mode frequency (kHz)	3.0	5.2	7.4	9.5	12	16	20
Microwave determination of cavity radius	9.6	9.6	9.6	9.6	9.6	9.6	9.6
Fitting precision	0.5	0.3	0.2	0.4	0.4	2.7	4.4
Excess halfwidths	24	17	16	13	13	12	34
Shell coupling corrections	0.3	0.3	0.3	0.2	0.1	7.5	0.6
Experimental method (ppm)	**26**	**19**	**19**	**17**	**16**	**17**	**35**
Thermometry calibration	8.5	8.5	8.5	8.5	8.5	8.5	8.5
Thermometry resistance measurements	42	42	42	42	42	42	42
Vertical temperature gradient	58	58	58	58	58	58	58
Relative humidity	80	80	80	80	80	80	80
CO_2 concentration	25	25	25	25	25	25	25
Environmental uncertainty (ppm)	**110**	**110**	**110**	**110**	**110**	**110**	**110**
Total relative (ppm)	**113**	**112**	**112**	**111**	**111**	**112**	**116**
Total (m s^{-1})	0.039	0.039	0.039	0.038	0.038	0.038	0.040

frequency range. Additionally, we observe that while the model predicts a relative dispersion of speed of sound between 3 kHz and 20 kHz on the order of 85 ppm, our determination of w_{exp} only approximately confirm the expected dispersion, with 65 ppm between w_{exp} measured by modes (0,2) and (0,10). However, we remark that such a discrepancy is commensurate to the 16 ppm relative standard uncertainty of the relaxation correction $K_r/2$ at 20 kHz, due to the combined contribution of its inherent defining parameters and the imperfect experimental determination of relative humidity.

As a whole, the experimental dataset acquired using the acoustic resonator comprises eight measurement runs for a total of 2036 measurement points, recorded while the environmental conditions of the test chamber spanned the following overall ranges: 284.7 K < T < 297.7 K, 99.45 kPa < p < 100.0 kPa, 32.7% < h_r < 60.8%, and 465 ppm < x_{CO2} < 600 ppm. From the complete dataset, 648

TABLE 9. Relative differences between experimental w_{exp} and calculated w_{theory} for selected measurements of speed of sound in humid air.

Record duration hours	Total meas. no.	Selected meas. no. $\lvert dT/dt \rvert < 1$ mK/min	T range $T_{min}-T_{max}$ (K)	Mean p (kPa)	Mean h_r (%)	Mean x_{CO2} (ppm)	Mode	$[(w_{exp}/w_{theory})]$ mean ± st. dev. (ppm)
13.9	139	59	293.4–293.5	100	54.9	536	(0,2) (0,10)	72 ± 13 50 ± 13
59.5	595	200	294.6–297.7	99.9	41.9	544	(0,2) (0,10)	104 ± 87 80 ± 80
9.2	93	4	284.7	99.7	62.3	561	(0,2) (0,10)	6 ± 16 −32 ± 13
15	150	96	291.9–292.4	99.7	46.0	550	(0,2) (0,10)	97 ± 65 70 ± 61
22.3	223	75	294.7	99.6	44.6	476	(0,2) (0,10)	6 ± 13 −11 ± 11
20.9	209	61	294.7–295.1	99.7	36.9	502	(0,2) (0,10)	−83 ± 48 −90 ± 47
7.9	79	4	291.4	99.6	36.6	561	(0,2) (0,10)	47 ± 20 27 ± 19
54.8	548	149	288.5–290.1	99.5	33.5	541	(0,2) (0,10)	13 ± 73 29 ± 68

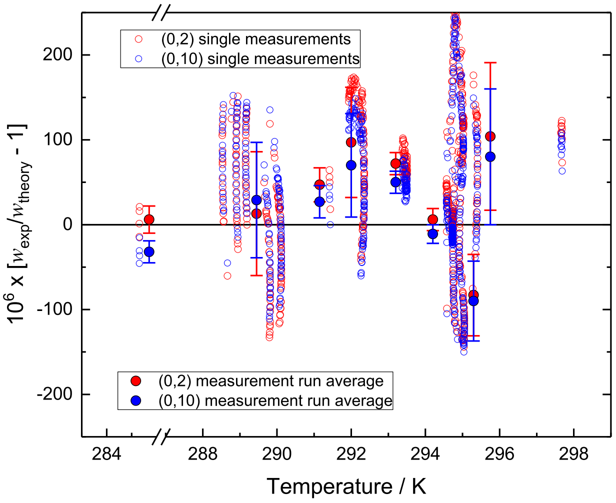

FIG. 20. Relative differences between experimental w_{exp} and calculated w_{theory} speed of sound in humid air for 648 measurements selected to comply with the thermal stability requirement $\lvert dT/dt \rvert \leq 1$ mK/min. Hollow circles display single measurement data for the mode (0,2) at 3.0 kHz (in red) and mode (0,10) at 20.0 kHz (in blue). Full circles and uncertainty bars display the mean and standard deviation of each measurement run considered in Table 9; the symbols are slightly offset on the temperature axis to enhance visual clarity.

measurements were selected by imposing the single condition that the variation of the resonator temperature with time $\lvert dT/dt \rvert$ be less than 1 mK/min. For these selected data (summarized in Table 9), the agreement between experiment and theory is illustrated in Fig. 20 for the lowest-frequency mode (0,2) and the highest-frequency mode (0,10) by plotting their relative difference from unity $[(w_{exp}/w_{theory}) - 1]$. For data groups belonging to the same measurement run, the mean and standard deviation of the same quantity is listed in the rightmost column of Table 9, and separately plotted in Fig. 20. Inclusion of all the measurement results in a single group leads to the overall mean estimate (49.3 ± 89.0) ppm for mode (0,2) and (36.6 ± 80.1) ppm for mode (0,10).

4.5. Mutual comparison of two experiments

In the preparation of the uncertainty budgets of the acoustic measurements obtained using the interferometer or the resonator, respectively discussed in Secs. 4.2 and 4.4, a distinction was made between uncertainty contributions related to the experiments themselves and those arising from the imperfect estimate of the environmental parameters in the test chamber. Because these parameters, which include relative humidity, CO_2 concentration, and temperature, were recorded contemporarily for both experiments using the same sensors and instrumentation, their uncertainties are fully correlated and they might be ignored in a direct comparison aimed at proving whether the two experiments were indeed

TABLE 10. Comparison of experimental determinations of speed of sound obtained with two different methods, respectively the wavelength meter w_{wave} operated at 20 kHz and mode (0,10) at very nearly the same frequency from the spherical resonator w_{res}. For both methods, the standard uncertainty u_{exp} includes contributions from various sources detailed as *experimental* in Tables 7 and 8 and, additionally, the contribution of a thermal gradient; the standard uncertainty u_{tot} also includes all other contributions detailed as *environmental* in Tables 7 and 8

T_{ref} (K)	p (kPa)	h_{r} (%)	x_{CO2} (ppm)	$w_{\mathrm{wave}} \pm u_{\mathrm{exp}}$ (m s^{-1})	$w_{\mathrm{res}} \pm u_{\mathrm{exp}}$ (m s^{-1})	$w_{\mathrm{wave}} \pm u_{\mathrm{tot}}$ (m s^{-1})	$w_{\mathrm{res}} \pm u_{\mathrm{tot}}$ (m s^{-1})	w_{theory} (m s^{-1})
293.45	99.98	54.8	538	344.242 ± 0.032	344.268 ± 0.020	344.242 ± 0.046	344.268 ± 0.038	344.2503 ± 0.0086
292.27	99.66	48.6	526	343.484 ± 0.032	343.432 ± 0.040	343.484 ± 0.045	343.432 ± 0.051	343.4469 ± 0.0089
294.60	99.54	44.5	473	344.865 ± 0.032	344.849 ± 0.021	344.865 ± 0.046	344.849 ± 0.038	344.8489 ± 0.0088
295.00	99.59	36.7	473	345.031 ± 0.032	344.952 ± 0.019	345.031 ± 0.046	344.952 ± 0.046	344.9976 ± 0.0092
291.50	99.56	37.1	550	342.906 ± 0.032	342.850 ± 0.032	342.906 ± 0.045	342.850 ± 0.038	342.8540 ± 0.0094
288.85	99.40	35.3	570	341.260 ± 0.032	341.198 ± 0.032	341.260 ± 0.045	341.198 ± 0.045	341.2220 ± 0.0091

consistent within their combined estimated uncertainties. Such a comparison is, however, limited to a subset of the full measurement record, for a minority of instances when measurements from the two experiments were contemporarily recorded, and the temperature of the resonator and that of the air sampled across the traveling path of the λ-meter were sufficiently close to each other and slowly variable as a function of time.

Table 10 reports the reference thermodynamic conditions considered for the calculation of w_{theory} and the comparison of the two experiments, respectively the wavelength meter w_{wave} and the resonator w_{res}, with measurement data from both experiments corrected for slight experimental temperature differences from the same reference T_{ref}. Measurements with the wavelength meter were taken at 20 kHz, allowing comparison with mode (0,10) results obtained with the resonator at very nearly the same frequency.

The standard uncertainty of the experiments has contributions from the sources previously listed in Tables 7 and 8, with the addition of the thermal gradient which is a relevant contribution to the uncertainty of w_{res}. Figure 21 shows the relative difference between w_{wave} and w_{res} and, for completeness, the difference of both from w_{theory}. Remarkably, w_{wave} and w_{res} are found in very good mutual agreement, in all cases within their combined standard experimental uncertainty. Also, in all cases, the experimental determinations from both experiments are found consistent with the predicted w_{theory} from the model discussed in Sec. 2.

5. Concluding Remarks and Future Perspectives

Taking advantage of the relevant progress achieved in the development of accurate reference sources for the thermodynamic properties of the main constituents of dry air and water vapor, we have revised and updated a model of speed of sound in humid air previously made available thanks to the outstanding, comprehensive work of Zuckerwar,[3] who set the theoretical and bibliographic grounds needed for the calculation of the speed of sound in air as a function of all the parameters of influence including temperature, pressure, composition, and frequency.

The model revision presented here is valid between 200 K and 647 K, for pressures up to 10 MPa, for arbitrary water vapor and CO_2 concentration and arbitrary acoustic frequency. The standard uncertainty of the model prediction of the speed of sound in air is as low as 25 ppm at ordinary, near-ambient conditions of temperature, pressure, and humidity (see Figs. 8 and 9), allowing, in principle, for a determination of T by acoustic thermometry in humid air accurate at the level of 50 ppm, i.e., with standard uncertainty of only 0.015 K near ambient temperature. To achieve such performance, it would be additionally required to maintain the uncertainty in the determination of relative humidity and CO_2 concentration respectively within $u(h_{\mathrm{r}}) = 0.5\%$, and $u(x_{\mathrm{CO2}}) = 80$ ppm, limits which would not be too demanding in most practical applications.

Further reduction of the model uncertainty awaits more accurate experimental determinations, or first-principle calculations, of the pure and interaction virial coefficient of air and water. The completeness and accuracy of the model would also be increased by including a correction to account for relaxation effects in CO_2. Also, because the model uncertainty significantly increases at high pressures, a formulation based on a Helmholtz equation of state may provide an interesting alternative in this range.

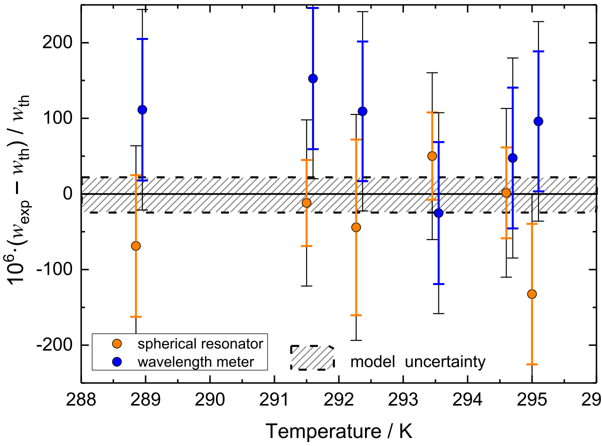

FIG. 21. Relative differences between experimental w_{exp} and calculated w_{theory} speed of sound in humid air for a subset of measurements obtained with the wavelength meter (blue) and the spherical resonator (orange). Measurements with the two experiments were corrected to the same reference temperature but are plotted slightly offset on the horizontal axis to facilitate their comparison. Inner (colored) uncertainty bars represent the standard uncertainty of each experiment. Outer (black) uncertainty bars include the uncertainty in the determination of the environmental parameters. The dashed shaded area represents the uncertainty of w_{theory}.

Our work was initially motivated by the possible application of acoustic thermometry in air to correct dimensional measurements with optical interferometry. Realization of a wavelength-measuring technique, combined with conventional thermometry, allowed comparing the experimentally determined speed of sound to the predictions of the thermodynamic model in a mutual validation process; the validation was limited by the uncertainty of the experiment, which is larger than the uncertainty of the model by a factor of four. A second experiment was implemented to contemporarily measure speed of sound using an acoustic resonator, a method that is well characterized and capable of high accuracy, here limited by its operation in the open environment of the test chamber instead of under accurately controlled laboratory conditions. Nevertheless, measurements carried out with the two experiments were found in remarkable agreement with each other—and with the model—confirming that the uncertainty budget of the interferometric technique was realistic. The imperfect determination of humidity and temperature in the test chamber limited the overall accuracy of the experiments at the level of (100–150) ppm, restricting the significance of the model validation, but demonstrating at the same level the use of acoustic thermometry for practical, accurate length metrology.

Laboratory measurements based on a combined acoustic/microwave resonator may lead in the future to experimental determinations of speed of sound in air as accurate as the current model predictions. In such experiments, the determination of the water mole fraction could be obtained by the microwave measurement of the refractive index of the mixture,[40,41] avoiding the inherent uncertainty contribution of humidity measurements.

6. Open Software Tools for Speed of Sound Calculation

In order to make our model calculation of speed of sound in air available for general use, we considered various alternatives. The derivation, by fitting modeled data, of an approximate equation explicit in its dependence on the environmental parameters, i.e., the choice implemented by Cramer,[52] did not seem to be a viable route due to the complication introduced by the inclusion in our model of frequency-dependent relaxation effects and the wide $(T, p, x_{\mathrm{w}}, x_{\mathrm{CO2}}, f)$ range of validity of the model itself. In fact, due to the same complications, Zuckerwar instead presented the results of his work as a voluminous collection of printed tables[3] that, in spite of being rather comprehensive, are not directly suitable for software implementation.

Because our model was developed for laboratory use, it was originally implemented using LabVIEW® (Laboratory Virtual Instrument Engineering Workbench), a development platform that uses a visual programming language produced and distributed by National Instruments. LabVIEW is available for all the most widespread operating systems and, more importantly, it allows for the open distribution of executable files which do not require a proprietary license to be run, but only the previous installation of the freely available LabVIEW Run-Time Engine executable.

All the original source (*.vi) files developed for the calculation of the thermodynamic properties of the constituents of dry air and water vapor, as needed to implement our model of speed of sound, are freely available.[81] In the same public repository, we also made available three main source files and the corresponding executable (*.exe) versions, namely:

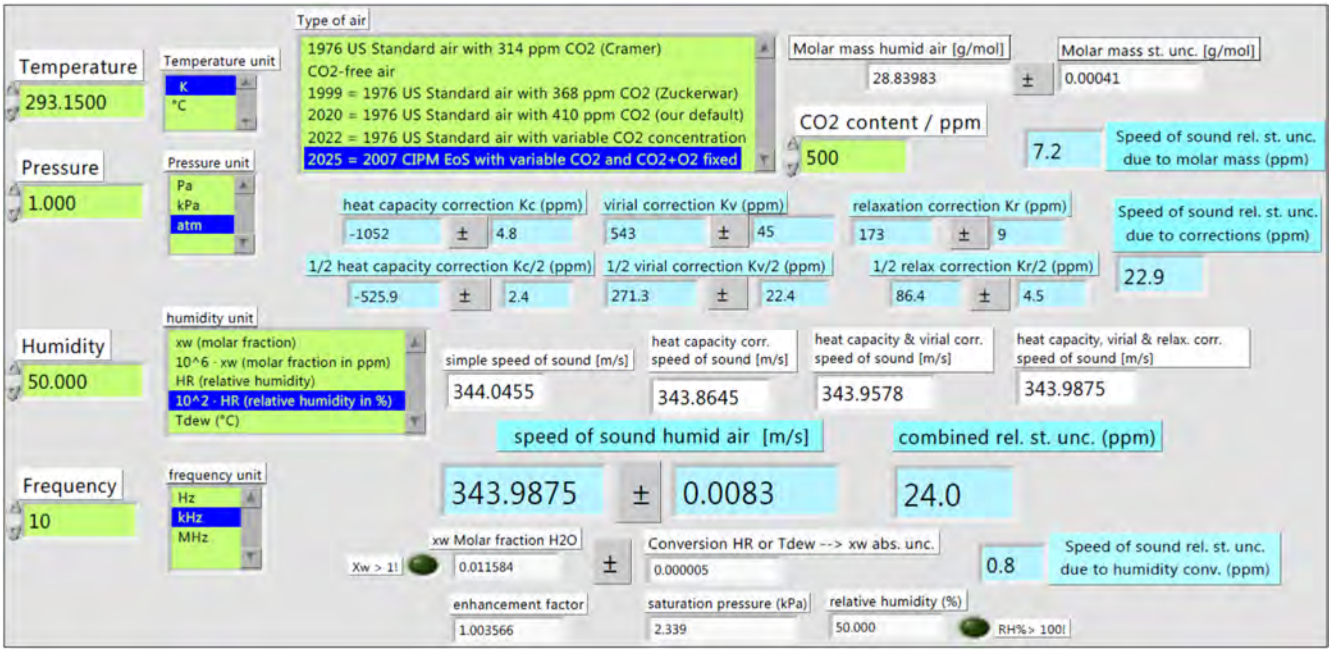

Temperature 293.1500
Temperature unit K
Pressure 1.000
Pressure unit atm
Humidity 50.000
humidity unit 10^2 · HR (relative humidity in %)
Frequency 10
frequency unit kHz
Type of air 2025 = 2007 CIPM EoS with variable CO2 and CO2+O2 fixed
Molar mass humid air [g/mol] 28.83983 ± 0.00041
Molar mass st. unc. [g/mol] 0.00041
CO2 content / ppm 500
Speed of sound rel. st. unc. due to molar mass (ppm) 7.2
heat capacity correction Kc (ppm) -1052 ± 4.8
virial correction Kv (ppm) 543 ± 45
relaxation correction Kr (ppm) 173 ± 9
Speed of sound rel. st. unc. due to corrections (ppm) 22.9
1/2 heat capacity correction Kc/2 (ppm) -525.9 ± 2.4
1/2 virial correction Kv/2 (ppm) 271.3 ± 22.4
1/2 relax correction Kr/2 (ppm) 86.4 ± 4.5
simple speed of sound [m/s] 344.0455
heat capacity corr. speed of sound [m/s] 343.8645
heat capacity & virial corr. speed of sound [m/s] 343.9578
heat capacity, virial & relax. corr. speed of sound [m/s] 343.9875
speed of sound humid air [m/s] 343.9875 ± 0.0083
combined rel. st. unc. (ppm) 24.0
xw Molar fraction H2O 0.011584 ±
Conversion HR or Tdew --> xw abs. unc. 0.000005
Speed of sound rel. st. unc. due to humidity conv. (ppm) 0.8
enhancement factor 1.003566
saturation pressure (kPa) 2.339
relative humidity (%) 50.000

FIG. 22. Screenshot of Labview software implementing the modeled calculation of speed of sound in humid air.

- SoS_AIR_2025.exe - This software (screenshot in Fig. 22) outputs speed of sound in humid air and its standard uncertainty given the input parameters T, p, h_r, x_{CO2}, f. Additional control inputs allow choosing among several alternative units for these parameters. Additional outputs include the contribution of the heat capacity, virial, and relaxation corrections and their respective uncertainties, humidity conversion parameters and their uncertainties with warning indicators if an incorrect choice of the input parameters leads to saturation conditions and/or water mole fraction exceeding unity.
- Plot & Save SoS.exe - This software allows users to create plots and save in tabular form text files listing speed of sound in humid air and its standard uncertainty given an arbitrary choice to fix at constant value two out of four of the input parameters T, p, h_r, f and to let one of the remaining parameters vary, with arbitrary resolution, between limiting bounds. The fourth parameter can also vary at discrete interleaved intervals between arbitrary bounds to create multiple traces on the same plot. The CO_2 concentration must be fixed to a constant value. The example screenshot in Fig. 23 reproduces the software settings to prepare the data previously plotted in Fig. 1, with T = 293.15 K, p = 1 atm, x_{CO2} = 368 ppm, h_r varying between 0% (dry air) and 12%, and f varying between 100 Hz and 1 kHz.
- T from SoS_AIR_2025.exe - Given a value of experimentally measured speed of sound in air as input, for a specified set of parameters (p, h_r, x_{CO2}, f) this software calculates the corresponding acoustic temperature T by iteration, using a simple bisection method. An initial guess of T and the tolerance of the iterative calculation are additional required inputs. The screenshot in Fig. 24 shows its use for the same speed of sound, and the same set of parameters of influence listed in row 7 of Table 4.

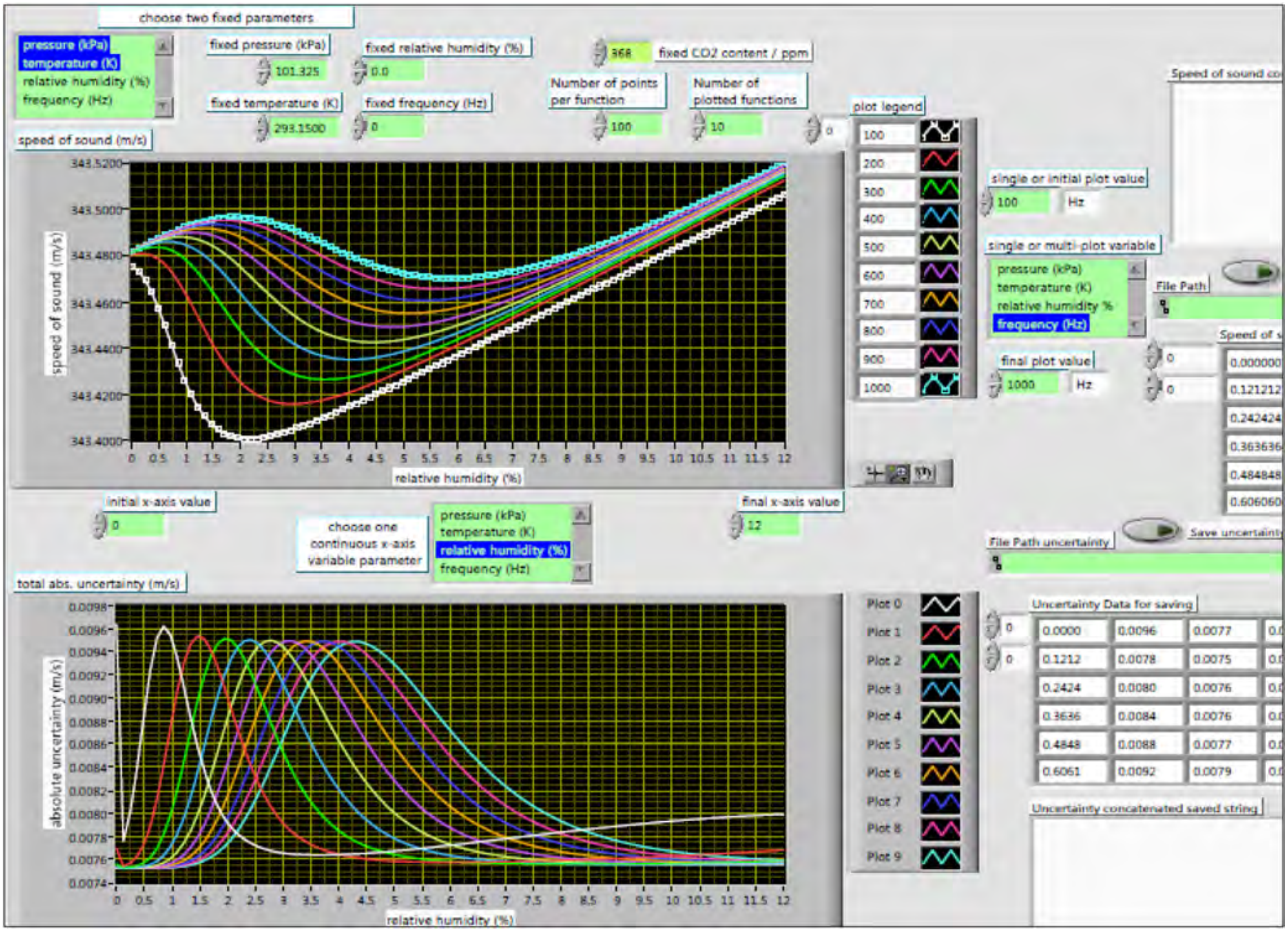

fixed pressure (kPa) 101.325

fixed relative humidity (%) 0.0

fixed temperature (K) 293.1500

fixed frequency (Hz) 0

368 fixed CO2 content / ppm

Number of points per function 100

Number of plotted functions 10

plot legend: 100, 200, 300, 400, 500, 600, 700, 800, 900, 1000

single or initial plot value 100 Hz

single or multi-plot variable: frequency (Hz)

final plot value 1000 Hz

initial x-axis value 0

final x-axis value 12

choose one continuous x-axis variable parameter: relative humidity (%)

0.000000
0.121212
0.242424
0.363636
0.484848
0.606060

Uncertainty Data for saving

0.0000	0.0096	0.0077
0.1212	0.0078	0.0075
0.2424	0.0080	0.0076
0.3636	0.0084	0.0076
0.4848	0.0088	0.0077
0.6061	0.0092	0.0079

FIG. 23. Screenshot of Labview software used to plot and save datasets for multiple calculated values of speed of sound in humid air.

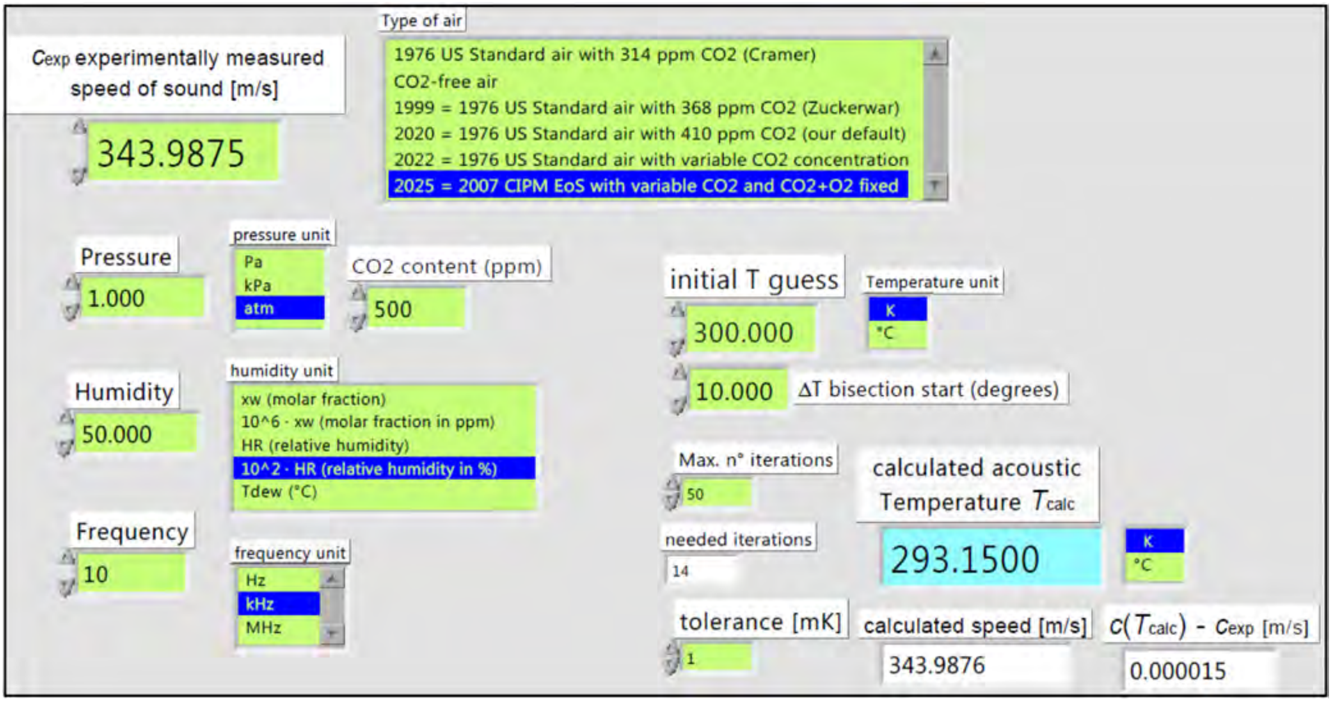

Cexp experimentally measured speed of sound [m/s]: 343.9875

Type of air: 2025 = 2007 CIPM EoS with variable CO2 and CO2+O2 fixed

Pressure: 1.000

pressure unit: atm

CO2 content (ppm): 500

initial T guess: 300.000

Temperature unit: K

10.000 ΔT bisection start (degrees)

Humidity: 50.000

humidity unit: 10^2 · HR (relative humidity in %)

Max. n° iterations: 50

needed iterations: 14

calculated acoustic Temperature Tcalc: 293.1500 K

Frequency: 10

frequency unit: kHz

tolerance [mK]: 1

calculated speed [m/s]: 343.9876

c(Tcalc) - Cexp [m/s]: 0.000015

FIG. 24. Screenshot of Labview software used to calculate acoustic temperature from an experimental estimate of speed of sound.

Acknowledgments

We are grateful to Allan Harvey for suggesting relevant improvements to this work, particularly concerning recent progress in the calculation of ideal gas heat capacities and other thermodynamic properties of air constituents. Encouragement from the late Mike Moldover and from Laurent Pitre in the course of this work was an important source of motivation.

7. Author Declarations

7.1. Conflict of interest

The authors have no conflicts to disclose.

8. Data Availability

The data that support the findings of this study are available within the article.

9. References

[1] M. Pisani, M. Astrua, and M. Zucco, "An acoustic thermometer for air refractive index estimation in long distance interferometric measurements," Metrologia **55**, 67 (2018).

[2] R. Richiardone, M. Manfrin, S. Ferrarese, C. Francone, V. Fernicola, R. M. Gavioso, and L. Mortarini, "Influence of the sonic anemometer temperature calibration on turbulent heat-flux measurements," Boundary-Layer Meteorol. **142**, 425 (2012).

[3] A. J. Zuckerwar, *Handbook of the Speed of Sound in Real Gases – Volume III Speed of Sound in Air* (Academic Press, London, 2002).

[4] M. R. Moldover, R. M. Gavioso, J. B. Mehl, L. Pitre, M. de Podesta, and J. T. Zhang, "Acoustic gas thermometry," Metrologia **51**, R1 (2014).

[5] K. A. Gillis and M. R. Moldover, "Practical determination of gas densities from the speed of sound using square-well potentials," Int. J. Thermophys. **17**, 1305 (1996).

[6] *U. S. Standard Atmosphere* (U.S. Government Printing Office Washington, DC, 1976).

[7] S. Y. Park, J. S. Kim, J. B. Lee, M. B. Esler, R. S. Davis, and R. I. Wielgosz, "A redetermination of the argon content of air for buoyancy corrections in mass standard comparisons," Metrologia **41**, 387 (2004).

[8] A. Picard, R. S. Davis, M. Gläser, and K. Fujii, "Revised formula for the density of moist air (CIPM-2007)," Metrologia **45**, 149 (2008).

[9] T. Prohaska, J. Irrgeher, J. Benefield J. K. Böhlke, L. A. Chesson, T. B. Coplen, T. Ding, P. J. H. Dunn, M. Gröning, N. E. Holden, H. A. J. Meijer, H. Moossen, A. Possolo, Y. Takahashi, J. Vogl, T. Walczyk, J. Wang, M. E. Wieser, S. Yoneda, X.-K. Zhu, and J. Meija, "Standard atomic weights of the elements 2021 (IUPAC Technical Report)," Pure Appl. Chem. **94**, 573 (2022).

[10] T. B. Coplen and Y. Shrestha, "Isotope-abundance variations and atomic weights of selected elements: 2016 (IUPAC Technical Report)," Pure Appl. Chem. **88**, 1203 (2016).

[11] J. K. Böhlke, "Variation in the terrestrial isotopic composition and atomic weight of argon (IUPAC Technical Report)," Pure Appl. Chem. **86**, 1421 (2014).

[12] Y. S. Touloukian and T. Makita, *Specific Heat: Nonmetallic Liquids and Gases, Vol. 6 of Thermophysical Properties of Matter* (IFI/Plenum, New York, 1970).

[13] R. R. Gamache and N. G. Orphanos, "Thermodynamic functions for N_2 from the total partition sum and its moments," J. Phys. Chem. Ref. Data **52**, 023101 (2023).

[14] R. Span, E. W. Lemmon, R. T. Jacobsen, W. Wagner, and A. Yokozeki, "A reference equation of state for the thermodynamic properties of nitrogen for temperatures from 63.151 to 1000 K and pressures to 2200 MPa," J. Phys. Chem. Ref. Data **29**, 1361 (2000).

[15] M. B. Ewing and J. P. M. Trusler, "Second acoustic virial coefficient of nitrogen between 80 and 373 K," Physica A **184**, 415 (1992).

[16] M. F. Costa Gomes and J. P. M. Trusler, "The speed of sound in nitrogen at temperatures between $T = 250$ K and $T = 350$ K and at pressures up to 30 MPa," J. Chem. Thermodyn. **30**, 527 (1998).

[17] T. Furtenbacher, M. Horváth, D. Koller, P. Sólyom, A. Balogh, I. Balogh, and A. G. Császár, "MARVEL analysis of the measured high-resolution rovibronic spectra and definitive ideal-gas thermochemistry of the $^{16}O_2$ molecule," J. Phys. Chem. Ref. Data **48**, 023101 (2019).

[18] E. Tiesinga, P. J. Mohr, D. B. Newell, and B. N. Taylor, "CODATA recommended values of the fundamental physical constants: 2018," Rev. Mod. Phys. **93**, 025010 (2021).

[19] T. Furtenbacher, A. H. Harvey, and A. G. Császár, "Improved partition functions and related thermochemical quantities for the $^{16}O_2$ and $H_2{}^{16}O$ molecules," J. Phys. Chem. Ref. Data **54**, 033103 (2025).

[20] S. A. Tashkun and A. H. Harvey, "Partition functions and ideal-gas thermodynamics for carbon dioxide," J. Phys. Chem. Ref. Data **54**, 023102 (2025).

[21] E. W. Lemmon, A. H. Harvey, and R. Hellmann, "Alternative fundamental equation of state for fluid carbon dioxide," NIST Internal Report, 2025 (in press).

[22] U. Setzmann and W. Wagner, "A new equation of state and tables of thermodynamic properties for methane covering the range from the melting line to 625 K at pressures up to 1000 MPa," J. Phys. Chem. Ref. Data **20**, 1061 (1991).

[23] W. Wagner and A. Pruß, "The IAPWS formulation 1995 for the thermodynamic properties of ordinary water substance for general and scientific use," J. Phys. Chem. Ref. Data **31**, 387 (2002).

[24] J. Hilsenrath, C. W. Beckett, W. S. Benedict, L. Fano, H. J. Hoge, J. F. Masi, R. L. Nuttall, Y. S. Touloukian, and H. W. Woolley, *Tables of Thermal Properties of Gases*, *National Bureau of Standards Circular No. 564* (U.S. Government Printing Office Washington, DC, 1955).

[25] J. M. H. Levelt Sengers, M. Klein, and J. S. Gallagher, in *American Institute of Physics Handbook*, edited by D. E. Gray (McGraw-Hill, New York, 1972).

[26] V. V. Sychev, A. A. Vasserman, A. D. Kozlov, G. A. Spiridonov, and V. A. Tsymarny, *Thermodynamic Properties of Air* (Hemisphere, Washington, DC, 1988).

[27] R. S. Davis, "Equation for the determination of the density of moist air (1981/91)," Metrologia **29**, 67 (1992).

[28] E. W. Lemmon, R. T. Jacobsen, S. G. Penoncello, and D. G. Friend, "Thermodynamic properties of air and mixtures of nitrogen, argon, and oxygen from 60 to 2000 K at pressures to 2000 MPa," J. Phys. Chem. Ref. Data **29**, 331 (2000).

[29] J. H. Dymond and E. B. Smith, *The Virial Coefficients of Pure Gases and Mixtures* (Oxford University Press, Oxford, 1980).

[30] E. W. Lemmon, I. H. Bell, M. L. Huber, and M. O. McLinden, *NIST Standard Reference Database 23: Reference Fluid Thermodynamic and Transport Properties*, Version 10.0 (Standard Reference Data Program National Institute of Standards and Technology, Gaithersburg, MD, 2018).

[31] A. H. Harvey and E. W. Lemmon, "Correlation for the second virial coefficient of water," J. Phys. Chem. Ref. Data **33**, 369 (2004).

[32] G. Garberoglio, P. Jankowski, K. Szalewicz, and A. H. Harvey, "Fully quantum calculation of the second and third virial coefficients of water and its isotopologues from *ab initio* potentials," Faraday Discuss. **212**, 467 (2018).

[33] R. Hellmann, "Reference values for the cross second virial coefficients and dilute gas binary diffusion coefficients of the systems ($H_2O + O_2$) and (H_2O + air) from first principles," J. Chem. Eng. Data **65**, 4130 (2020).

[34] A. H. Harvey and P. H. Huang, "First-principles calculation of the air–water second virial coefficient," Int. J. Thermophys. **28**, 556 (2007).

[35] R. W. Hyland and A. Wexler, "Formulations for the thermodynamic properties of dry air from 173.15 K to 473.15 K, and of saturated moist air from 173.15 K to 372.15 K, at pressures to 5 MPa," ASHRAE Trans. **89**, 520 (1983).

[36] R. W. Hyland and E. A. Mason, "Third virial coefficient for air-water vapor mixtures," J. Res. Natl. Bur. Stand., Sect. A **71A**, 219 (1967).

[37] E. A. Mason and L. Monchick, "Survey of the equation of state and transport properties of moist gases," in *Humidity and Moisture*, edited by A. Wexler and W. A. Wildhack (Reinhold Publishing Corporation, New York, 1965), Vol. III.

[38] ANSI/ASA 51.26-2014 Standard, *Methods for Calculation of the Absorption of Sound by the Atmosphere*, edited by Acoustical Society of America (Standards Secretariat, Acoustical Society of America, Melville, NY, 2014).

[39] H. E. Bass, "Absorption of sound by air: High temperature predictions," J. Acoust. Soc. Am. **69**, 124 (1981).

[40] R. Cuccaro, R. M. Gavioso, G. Benedetto, D. Madonna Ripa, V. Fernicola, and C. Guianvarc'h, "Microwave determination of water mole fraction in humid gas mixtures," Int. J. Thermophys. **33**, 1352 (2012).

[41] R. J. Underwood, R. Cuccaro, S. Bell, R. M. Gavioso, D. Madonna Ripa, M. Stevens, and M. de Podesta, "A microwave resonance dew-point hygrometer," Meas. Sci. Technol. **23**, 085905 (2012).

[42] W. Wagner and A. Pruß, "International equations for the saturation properties of ordinary water substance. Revised according to the International Temperature Scale of 1990. Addendum to J. Phys. Chem. Ref. Data 16, 893 (1987)," J. Phys. Chem. Ref. Data **22**, 783 (1993).

[43] D. Sonntag, "Important new values of the physical constants of 1986, vapour pressure formulations based on the ITS-90, and psychrometer formulae," Z. Meteorol. **40**, 340 (1990).

[44] L. Haar, J. S. Gallagher, and G. S. Kell, *NBS/NRC Steam Tables* (Hemisphere, New York, 1984).

[45] W. Wagner, T. Riethmann, R. Feistel, and A. H. Harvey, "New equations for the sublimation pressure and melting pressure of H_2O ice Ih," J. Phys. Chem. Ref. Data **40**, 043103 (2011).

[46] J. Lovell-Smith, "The propagation of uncertainty for humidity calculations," Metrologia **46**, 607 (2009).

[47] R. W. Hyland, "A correlation for the second interaction virial coefficients and enhancement factors for moist air," J. Res. Natl. Bur. Stand., Sect. A **79A**, 551 (1975).

[48] L. Greenspan, "Functional equations for the enhancement factors for CO_2-free moist air," J. Res. Natl. Bur. Stand., Sect. A **80A**, 41 (1976).

[49] B. Hardy, "ITS-90 formulations for vapor pressure, frostpoint temperature, dewpoint temperature, and enhancement factors in the range −100 to +100 °C," in Proceedings of the Third International Symposium on Humidity and Moisture, Teddington; London, England, 1998.

[50] A. J. Zuckerwar, *Handbook of the Speed of Sound in Real Gases – Vol. I Theory* (Academic Press, London, 2002).

[51] A. J. Zuckerwar and R. W. Meredith, "Low-frequency absorption of sound in air," J. Acoust. Soc. Am. **78**, 946 (1985).

[52] O. Cramer, "The variation of the specific heat ratio and the speed of sound in air with temperature, pressure, humidity, and CO_2 concentration," J. Acoust. Soc. Am. **93**, 2510 (1993).

[53] D. H. Smith and R. G. Harlow, "The velocity of sound in air, nitrogen and argon," Br. J. Appl. Phys. **14**, 102 (1963).

[54] M. B. Ewing and A. R. H. Goodwin, "Speeds of sound, perfect-gas heat capacity, and second acoustic virial coefficient for air at the temperature 255 K and pressures in the range 0.031 MPa to 6.9 MPa," J. Chem. Thermodyn. **25**, 423 (1993).

[55] J. P. M. Trusler, *Physical Acoustics and Metrology of Fluids* (Adam Hilger, Bristol, 1991).

[56] G. S. K. Wong, "Speed of sound in standard air," J. Acoust. Soc. Am. **79**, 1359 (1985).

[57] V. Korpelainen and A. Lassila, "Acoustic method for determination of the effective temperature and refractive index of air in accurate length interferometry," Opt. Eng. **43**, 2400 (2004).

[58] R. Przybyla, A. Flynn, V. Jain, S. Shelton, A. Guedes, I. Izyumin, D. Horsley, and B. Boser, "A micromechanical ultrasonic distance sensor with >1 meter range," in 2011 16th International Solid-State Sensors, Actuators and Microsystems Conference, Beijing, China, 2070.

[59] G. Benedetto, R. M. Gavioso, P. A. Giuliano Albo, S. Lago, D. Madonna Ripa, and R. Spagnolo, "Speed of sound in pure water at temperatures between 274 and 394 K and at pressures up to 90 MPa," Int. J. Thermophys. **26**, 1667 (2005).

[60] T. Dietl, A. El Hawary, R. M. Gavioso, R. Hellmann, and K. Meier, "Speed of sound measurements and derived third and fourth acoustic virial coefficients of supercritical neon," Metrologia **61**, 045007 (2024).

[61] M. R. Moldover, J. B. Mehl, and M. Greenspan, "Gas-filled spherical resonators: Theory and experiment," J. Acoust. Soc. Am. **79**, 253 (1986).

[62] J. B. Mehl and M. R. Moldover, "Measurement of the ratio of the speed of sound to the speed of light," Phys. Rev. A **34**, 3341 (1986).

[63] M. Pisani, M. Astrua, and A. Merlone, "Non-contact thermometer for improved air temperature measurements," Sensors **23**, 1908 (2023).

[64] P. J. Fox, R. E. Scholten, M. R. Walkiewicz, and R. E. Drullinger, "A reliable, compact, and low-cost Michelson wavemeter for laser wavelength measurement," Am. J. Phys. **67**, 624 (1999).

[65] R. M. Gavioso, G. Benedetto, P. A. Giuliano Albo, D. Madonna Ripa, A. Merlone, C. Guianvarc'h, F. Moro, and R. Cuccaro, "A determination of the Boltzmann constant from speed of sound measurements in helium at a single thermodynamic state," Metrologia **47**, 387 (2010).

[66] M. de Podesta, E. F. May, J. B. Mehl, L. Pitre, R. M. Gavioso, G. Benedetto, P. A. Giuliano Albo, D. Truong, and D. Flack, "Characterization of the volume and shape of quasi-spherical resonators using coordinate measurement machines," Metrologia **47**, 588 (2010).

[67] R. M. Gavioso, D. Madonna Ripa, P. P. M. Steur, C. Gaiser, D. Truong, C. Guianvarc'h, P. Tarizzo, F. M. Stuart, and R. Dematteis, "A determination of the molar gas constant *R* by acoustic thermometry in helium," Metrologia **52**, S274 (2015).

[68] SI Brochure (9th ed) Appendix 2 (MeP-K), https://www.bipm.org/en/publications/mises-en-pratique, 2019.

[69] J. B. Mehl, "Second-order electromagnetic eigenfrequencies of a triaxial ellipsoid," Metrologia **46**, 554 (2009).

[70] R. M. Gavioso, G. Benedetto, P. A. Giuliano Albo, A. Merlone, A. Balsamo, G. E. D'Errico, and R. Spagnolo, "Progress towards an acoustic measurement of the molar gas constant at INRIM," Int. J. Thermophys. **28**, 1775 (2007).

[71] R. J. Underwood, J. B. Mehl, L. Pitre, G. Edwards, G. Sutton, and M. de Podesta, "Waveguide effects on quasispherical microwave cavity resonators," Meas. Sci. Technol. **21**, 075103 (2010).

[72] J. B. Mehl, "Acoustic eigenvalues of a quasispherical resonator: Second order shape perturbation theory for arbitrary modes," J. Res. Natl. Inst. Stand. Technol. **112**, 163 (2007).

[73] S. G. S. Beirão, A. P. C. Ribeiro, M. J. V. Lourenço, F. J. V. Santos, and C. A. Nieto de Castro, "Thermal conductivity of humid air," Int. J. Thermophys. **33**, 1686 (2012).

[74] A. Melling, S. Noppenberger, M. Still, and H. Venzke, "Interpolation correlations for fluid properties of humid air in the temperature range 100 °C to 200 °C," J. Phys. Chem. Ref. Data **26**, 1111 (1997).

[75] E. W. Lemmon and R. T. Jacobsen, "Viscosity and thermal conductivity equations for nitrogen, oxygen, argon, and air," Int. J. Thermophys. **25**, 21 (2004).

[76] W. M. Trott, J. N. Castañeda, J. R. Torczynski, M. A. Gallis, and D. J. Rader, "An experimental assembly for precise measurement of thermal accommodation coefficients, Rev. Sci. Instrum. **82**, 035120 (2011).

[77] J. B. Mehl, "Spherical acoustic resonator: Effects of shell motion," J. Acoust. Soc. Am. **78**, 782 (1985).

[78] H. M. Ledbetter, "Stainless-steel elastic constants at low temperatures," J. Appl. Phys. **52**, 1587 (1981).

[79] B. Edlén, "The refractive index of air," Metrologia **2**, 71 (1966).

[80] M. Dobosz and M. Ściuba, "Ultrasonic measurement of air temperature along the axis of a laser beam during interferometric measurement of length," Meas. Sci. Technol. **31**, 045202 (2020).

[81] See https://github.com/RobertoGavioso/Speed-of-sound-in-air for downloading executable and source file implementing the calculation of speed of sound in humid air.